

# Dynamical Properties of Two Coupled Hubbard Chains at Half-filling

H. Endres<sup>a</sup>, R.M. Noack<sup>a</sup>, W. Hanke<sup>a</sup>, D. Poilblanc<sup>b</sup>, and D.J. Scalapino<sup>c</sup>

*a) Institut für Theoretische Physik, Universität Würzburg,  
Am Hubland, 97074 Würzburg, Germany*

*b) Université Paul Sabatier, Laboratoire de Physique Quantique,  
118 route de Narbonne, 31062 Toulouse, France*

*c) Department of Physics, University of California, Santa Barbara, CA 93106*

Using grand canonical Quantum Monte Carlo (QMC) simulations combined with Maximum Entropy analytic continuation, as well as analytical methods, we examine the one- and two-particle dynamical properties of the Hubbard model on two coupled chains at half-filling. The one-particle spectral weight function,  $A(\mathbf{k}, \omega)$ , undergoes a qualitative change with interchain hopping  $t_{\perp}$  associated with a transition from a four-band insulator to a two-band insulator. A simple analytical model based on the propagation of exact rung singlet states gives a good description of the features at large  $t_{\perp}$ . For smaller  $t_{\perp}$ ,  $A(\mathbf{k}, \omega)$  is similar to that of the one-dimensional model, with a coherent band of width the effective antiferromagnetic exchange  $J$  reasonably well-described by renormalized spin-wave theory. The coherent band rides on a broad background of width several times the parallel hopping integral  $t$ , an incoherent structure similar to that found in calculations on both the one- and two-dimensional models. We also present QMC results for the two-particle spin and charge excitation spectra, and relate their behavior to the rung singlet picture for large  $t_{\perp}$  and to the results of spin-wave theory for small  $t_{\perp}$ .

## I. INTRODUCTION

The compounds  $\text{SrCu}_2\text{O}_3$ <sup>1</sup> and  $(\text{VO})_2\text{P}_2\text{O}_7$ <sup>2</sup> consist of arrays of weakly interacting two-chain metal-oxide ladders. In  $\text{SrCu}_2\text{O}_3$ ,  $\text{CuO}_2$  ladders are coupled by a weak, frustrated, ferromagnetic coupling<sup>3</sup>, and in  $(\text{VO})_2\text{P}_2\text{O}_7$ ,  $\text{VO}_4$  ladders are well separated in the structure of the material. These materials have a half-filled conduction band, corresponding to one conduction electron per metal-oxide unit and are insulators with short-range antiferromagnetic correlations and a spin gap. Very recently Z. Hiroi and M. Takano<sup>4</sup> succeeded in doping the two-leg ladder compound  $\text{La}_{1-x}\text{Sr}_x\text{CuO}_2$ . They observe a fall in resistivity with doping, possibly to a metallic state, but no sign of superconductivity. The spin-gap found in half-filled  $\text{LaCuO}_2$  persists, but decreases with doping. In this publication we will address the half-filled situation only. The undoped materials have been described by a Heisenberg model on two coupled chains<sup>3,5-7</sup>, which explains a number of experimentally observed magnetic properties of the materials, including the size of the spin gap, and the spectrum of the spin triplet excitations. The Hubbard model on two coupled chains, which at half-filling and in the limit of strong on-site Coulomb repulsion can be mapped onto the Heisenberg model, gives an itinerant electron picture of these systems<sup>8</sup> which includes charge as well as spin fluctuations. While the ground state and the low-energy properties of the two-chain Heisenberg and half-filled Hubbard model are becoming well understood, less is known about the finite frequency one- and two-particle response. The dynamic spin response of the Heisenberg model was studied in Ref. 5 and the single particle and spin response was

examined for a  $t$ - $J$  model with two holes in Ref. 8 using analytic continuation of Lanczos exact diagonalization calculations on small clusters. The dynamic properties are important because they can be measured with a variety of experimental techniques. For example, the one-particle spectral weight can be probed by photoemission and inverse photoemission, the dynamic charge correlation function by optical response measurements, and the dynamic spin structure factor by inelastic neutron scattering.

Here we examine the dynamic one- and two-particle correlation functions of the two-chain Hubbard model at half-filling using Quantum Monte Carlo simulations analytically continued to real frequencies using a Maximum Entropy technique<sup>10</sup>. We study the dynamic response for large, intermediate, and small values of the perpendicular hopping  $t_{\perp}$ . This is interesting for two reasons: first, when the electron-electron interaction is turned off ( $U = 0$ ) in the two-chain system, there is a metal-insulator transition from a two-band metal to a band insulator due to the separation of the bonding and antibonding bands with increasing  $t_{\perp}$ . For the interacting ( $U \neq 0$ ) case, it is generally believed that the two-chain system is always insulating (see, for example, Ref. 11 for a discussion within a weak-coupling RG picture). The QMC simulations do find an insulator for all  $t_{\perp}$ , but also reveal a crossover from four-band insulating behavior for small  $t_{\perp}$  to two-band behavior for  $t_{\perp}/t \gtrsim 2$ . A similar crossover occurs for weak coupling ( $U \lesssim t$ ) within antiferromagnetic Hartree-Fock (AFHF) theory, as we shall discuss in section II B. One interesting and important result of this paper is that this four-band to two-band crossover scenario survives in the interme-

diate to large  $U$  regime in the system, despite the fact that the many-body physics for  $t_{\perp} \gtrsim t$  is not even qualitatively reproduced in the AFHF approximation. No such crossover is present as a function of  $J_{\perp}/J$  in the Heisenberg model, because the mapping to the Heisenberg model breaks down when  $J_{\perp} \sim 4t_{\perp}^2/U$  is of the order of  $t_{\perp}$ . In other words, the effect of the electronic band structure is not present in the Heisenberg model. As we shall see, this crossover can also be described in terms of the crossover from a localized rung picture, in which localized excitations form a Bloch state along the chains for large  $t_{\perp}$ , to a picture with longer range anti-ferromagnetic correlations with many features that can be qualitatively described by AFHF spin-wave theory for small  $t_{\perp}$ .

Secondly, in the small to intermediate  $t_{\perp}$  regime, this system displays features of the single-particle spectral weight  $A(\mathbf{k}, \omega)$  seen in recent numerical treatments of both the 1D<sup>12,13</sup> and 2D<sup>14,15</sup> Hubbard model. We find two features also generic to the 1D and 2D systems: a dispersive band whose width is of the order of the effective exchange interaction  $J \sim 4t^2/U$  and an incoherent background of width several times the parallel hopping integral  $t$ . For the one and two chain systems, but not the 2D system, the dispersive band is well described by renormalized spin-wave theory.

We consider the single band Hubbard model on two coupled chains of length  $L$ :

$$H = -t \sum_{i,\lambda\sigma} (c_{i,\lambda\sigma}^{\dagger} c_{i+1,\lambda\sigma} + h.c.) - t_{\perp} \sum_{i,\sigma} (c_{i,1\sigma}^{\dagger} c_{i,2\sigma} + h.c.) + U \sum_{i\lambda} n_{i,\lambda\uparrow} n_{i,\lambda\downarrow}. \quad (1)$$

Here  $c_{i,\lambda\sigma}^{\dagger}$  and  $c_{i,\lambda\sigma}$  create and annihilate electrons on rung  $i$  and chain  $\lambda$  with spin  $\sigma$ , respectively, the hopping integral parallel to the chains is  $t$ , the hopping between the chains  $t_{\perp}$ , and  $U$  is an on-site Coulomb interaction. We use periodic boundary conditions parallel to and open boundary conditions perpendicular to the chains.

The non-interacting,  $U = 0$ , Hamiltonian can be diagonalized by writing the hopping term in terms of bonding and antibonding states on a rung and Fourier-transforming parallel to the chains. The energy is then given by

$$\varepsilon_{\mathbf{k}} = -(2t \cos k + t_{\perp} \cos k_{\perp}) \quad (2)$$

with  $\mathbf{k} = (k, k_{\perp})$ , where  $k_{\perp} = 0$  and  $k_{\perp} = \pi$  corresponds to the energy of the bonding and antibonding band, respectively, and  $k$  is the momentum along the chains. Both bands will be occupied when  $t_{\perp} < t_{\perp c}$ , whereas when  $t_{\perp} > t_{\perp c}$ , only the bonding band will be occupied. Here  $t_{\perp c}/t \equiv 1 - \cos \pi \langle n \rangle$  and  $\langle n \rangle \equiv \langle \sum_{\sigma} c_{i,\lambda,\sigma}^{\dagger} c_{i,\lambda,\sigma} \rangle$ . For half-filling  $t_{\perp c}/t = 2$ , and the system is a two-band metal for  $t_{\perp}/t < 2$ , and a band insulator with a completely occupied bonding band for  $t_{\perp}/t > 2$ .

## II. SINGLE-PARTICLE SPECTRAL WEIGHT

### A. Quantum Monte Carlo Results

In order to calculate the dynamical properties of the above model we employ the grand-canonical Quantum Monte Carlo (QMC) algorithm to determine the expectation values of the correlation functions in imaginary time. At half-filling, the simulations are not limited by the fermion sign problem and accurate results can thus be achieved at low temperatures and large system sizes. We analytically continue the imaginary-time data to real frequencies using a Maximum Entropy method<sup>10</sup>. For example, the spectral weight function given by

$$A(\mathbf{k}, \omega) = \frac{1}{Z} \sum_{l,l'} e^{-\beta E_l} (1 + e^{-\beta \omega}) |\langle l | c_{\mathbf{k},\uparrow} | l' \rangle|^2 \cdot \delta(\omega - (E_{l'} - E_l)), \quad (3)$$

where  $Z$  is the partition function,  $|l\rangle$  and  $|l'\rangle$  are the exact many-body eigenstates with the corresponding energies  $E_l$  and  $E_{l'}$  and  $c_{\mathbf{k},\sigma} = \sum_{i,\lambda} c_{i,\lambda\sigma} e^{i\mathbf{k}\cdot\mathbf{R}_{i,\lambda}} / \sqrt{2L}$ , can be calculated by inverting the spectral theorem

$$G(\mathbf{k}, \tau) \equiv \langle c_{\mathbf{k},\uparrow}(\tau) c_{\mathbf{k},\uparrow}^{\dagger}(0) \rangle = \int_{-\infty}^{\infty} \frac{e^{-\tau\omega}}{1 + e^{-\beta\omega}} A(\mathbf{k}, \omega) d\omega \quad (4)$$

with the Maximum Entropy algorithm using the raw QMC data  $G(\mathbf{k}, \tau)$ . To achieve high resolution, it is important to use a likelihood function which takes the error-covariance matrix of the QMC data and its statistical inaccuracy consistently into account<sup>16</sup>. The results presented here are based on QMC data with good statistics, i.e. averages over  $10^5$  updates of all the Hubbard-Stratonovich variables result in  $G(\mathbf{k}, \tau)$ 's with absolute errors less than or of the order of  $5 \times 10^{-4}$ . Correlations of the data in imaginary time were taken into account by making use of the covariance matrix in the Maximum Entropy procedure<sup>16</sup>. As suggested in previous work by White<sup>17</sup>, various moments of the spectral weight were also incorporated in extracting  $A(\mathbf{k}, \omega)$ .

We calculate the spectral function  $A(\mathbf{k}, \omega)$  at half-filling for a  $2 \times 16$ -lattice with  $U/t = 8$  for different values of  $t_{\perp}$  at an inverse temperature of  $\beta = 10/t$ . Our results are given in Fig. 1 for  $t_{\perp}/t = 2.0$ , in Fig. 2 for  $t_{\perp}/t = 1.0$ , and in Fig. 3 for  $t_{\perp}/t = 0.5$ . Note that  $t_{\perp}/t = 1.0$  corresponds to the isotropic case,  $J_{\perp} \approx J$ , relevant to the SrCu<sub>2</sub>O<sub>3</sub>, (VO)<sub>2</sub>P<sub>2</sub>O<sub>7</sub>, and LaCuO<sub>2.5</sub> compounds. Parts (a) and (b) in Fig. 1–3 are three-dimensional plots of  $A(\mathbf{k}, \omega)$  versus  $\omega$  for  $k$ -values in the 1D Brillouin zone, whereas part (c) in all three figures summarize these results in the usual “band structure”  $\omega$  versus  $k$  plot. The shaded areas represent regions

with significant spectral weight, with the darker shading representing more weight. Due to particle-hole symmetry,  $A(\mathbf{k} = (k, \pi), \omega) = A(\mathbf{k} = (\pi - k, 0), -\omega)$  where  $\mathbf{k} = (k, k_\perp)$ . In other words, one reflects  $k$  about  $k = \pi/2$  and  $\omega$  about 0 to get  $A(\mathbf{k}, \omega)$  for  $k_\perp = \pi$  from  $A(\mathbf{k}, \omega)$  for  $k_\perp = 0$ . This symmetry can be seen by comparing parts (a) and (b) of Fig. 1–3. Since this symmetry is not enforced by the Maximum Entropy procedure, it is only present approximately, and the extent to which the reflected spectra at  $k_\perp = 0$  do not match those at  $k_\perp = \pi$  gives an indication of the accuracy of the analytic continuation procedure. In the density plots in parts (c), we show only the  $k_\perp = 0$  components. For  $t_\perp/t = 2.0$ , there is a heavily weighted coherent band of width  $\sim 3t$  in the photoemission ( $\omega < 0$ ) part of the spectrum. In the inverse photoemission spectrum ( $\omega > 0$ ) there is very little total spectral weight. There are therefore two bands with significant spectral weight, one in the photoemission spectrum for  $k_\perp = 0$  and one in the inverse photoemission spectrum for  $k_\perp = \pi$ . Each band is about  $2t$  away from the Fermi surface, leading to a gap of approximately  $4t$ . Therefore, for large  $t_\perp$ , the system is a two-band insulator.

In contrast, for  $t_\perp/t = 1.0$  and  $t_\perp/t = 0.5$ ,  $A(\mathbf{k}, \omega)$  has substantial spectral weight in four bands, one in the photoemission spectrum ( $\omega < 0$ ) for  $k_\perp = 0$  and  $k_\perp = \pi$  and one in the inverse photoemission spectrum ( $\omega > 0$ ) for both values of  $k_\perp$ . In this regime, the system is thus a four-band insulator. For  $t_\perp/t = 0.5$  (Fig. 3) the spectral weight is present for both values of  $k_\perp$  concentrated between  $k = 0$  and  $k = \pi/2$  in the photoemission part and between  $k = \pi/2$  and  $k = \pi$  in the inverse photoemission part of the spectrum. For the isotropic case ( $t_\perp/t = 1.0$ , Fig. 2), there is some shift of spectral weight to the photoemission part for  $k_\perp = 0$  and to the inverse photoemission part for  $k_\perp = \pi$ . The maxima of the photoemission band in the  $k_\perp = 0$  part occurs at  $k^* = \pi$  for  $t_\perp/t = 2.0$ , at  $k^* \approx 0.7\pi$  for  $t_\perp/t = 1.0$ , and at  $k^* = \pi/2$  for  $t_\perp/t = 0.5$ . Therefore we would expect to see a maxima at  $k^* \approx 0.7\pi$  in a photoemission experiment on the isotropic ladder compounds, an experiment which has, to our knowledge, not yet been done.

It is also important to note that the QMC  $A(\mathbf{k}, \omega)$  results for  $t_\perp/t = 0.5$  as well as for the isotropic case,  $t_\perp/t = 1.0$ , display two general features which have recently been observed in both the 1D<sup>13</sup> and 2D<sup>14</sup> cases using the improved Maximum Entropy techniques described above<sup>16</sup>. One feature is that  $A(\mathbf{k}, \omega)$  contains a rather dispersionless “incoherent background” extending over several  $t$  ( $\sim 6t$  for  $U/t = 8$  in 2D) in both the electronically occupied ( $\omega < 0$ ) and unoccupied ( $\omega > 0$ ) parts of the spectrum. The crucial structure, not resolved in previous 1D and 2D QMC simulations, is a dispersive structure at low energies with a small width of the order of the exchange coupling  $J = 4t^2/U$ . It is this latter coherent “band” which defines the gap  $\Delta$  and which, for larger  $U$  ( $U/t \sim 10$ ), is well-separated from the higher-energy background. As in the 1D and

2D cases, the splitting in the low-energy band and the higher-energy background is especially pronounced near  $k = 0$  and  $k = \pi$  due to a relative weight shift from negative to positive energies as  $k$  moves through  $k^*$ .

## B. Spin-Wave Theory

At half-filling, the two chain Hubbard system at  $T = 0$  is a spin liquid with a spin gap and a finite spin-spin correlation length. The system is therefore less ordered than either the 1D system, which is at the critical point and has power law decay of the spin-spin correlation function and no spin gap, or the 2D system, which has long-range spin order and gapless spin-wave-like excitations. However, at large  $U/t$  the scale of the spin gap for the two chain system is set by  $J_\perp \sim 4t_\perp^2/U$ , and the spin-spin correlation length  $\xi$  grows longer as the spin gap gets smaller. The range of the spin ordering can therefore be tuned by varying  $t_\perp/t$ . This is illustrated by Fig. 4, in which we plot the spin-spin correlation function,  $S(r) = (-1)^r \langle M_{0,\lambda}^z M_{r,\lambda}^z \rangle$  on a semilog scale for  $t_\perp/t = 2.0$ ,  $t_\perp/t = 1.0$  and  $t_\perp/t = 0.5$ . Here  $M_{r,\lambda}^z = (n_{r,\lambda,\uparrow} - n_{r,\lambda,\downarrow})$  is twice the  $z$  component of the on-site spin. These calculations were done using the Density Matrix Renormalization Group method<sup>8</sup> (DMRG) on a system with open boundaries at zero temperature. For  $t_\perp/t = 0.5$ , the data was averaged over a number of different pairs of points for a given  $r$  in order to reduce oscillations due to the open boundaries. For distances greater than a few lattice spacings, the correlation functions are very well fit by a pure exponential form  $A \exp(-r/\xi)$ , from which the spin-spin correlation length  $\xi$  can be determined. For  $t_\perp/t = 2.0$ ,  $\xi = 0.83$ , for  $t_\perp/t = 1.0$ ,  $\xi = 4.3$ , and for  $t_\perp/t = 0.5$ ,  $\xi = 9.5$  lattice spacings. Therefore, the spins are almost completely uncorrelated along the chains for  $t_\perp/t = 2.0$ , but for  $t_\perp/t = 1.0$  and for  $t_\perp/t = 0.5$  are correlated on length scales of the order of the size of the  $2 \times 16$  lattice studied here, although the long-range behavior is that of a gapped spin liquid in all three cases.

It is therefore reasonable to calculate the single particle spectral weight  $A(\mathbf{k}, \omega)$  in two simple ways: first, when the spin gap is small and  $\xi \approx L$ , and we consider wavelengths smaller than  $\xi$  and frequencies larger than the spin gap, it is useful to explore the consequences of a simple SDW approximation based on an ordered state, i.e. AFHF theory. Secondly, one can solve for the exact eigenstates on a rung and then consider states composed of a product of exact rung singlets only and a delocalized one-hole state in a background of rung singlets. (We call this the Local Rung Approximation, LRA.) The LRA starts with a state with uncorrelated rungs and then treats the interactions between rungs perturbatively, and is thus a good starting point when  $\xi$  is small. As we shall see, the LRA gives a single particle spectral weight distribution that agrees well with QMC in the large  $t_\perp$  regime,

while AFHF qualitatively describes most features of the spectral weight distribution for small  $t_{\perp}$ .

We first discuss the AFHF calculation in more detail. The Hartree-Fock one-particle Hamiltonian can be written as

$$H_{HF} = \sum_{\mathbf{k},\sigma}' E_{\mathbf{k}} (b_{\mathbf{k},\sigma}^{c\dagger} b_{\mathbf{k},\sigma}^c - b_{\mathbf{k},\sigma}^{v\dagger} b_{\mathbf{k},\sigma}^v), \quad (5)$$

where  $\sum_{\mathbf{k},\sigma}'$  means that the sum runs only over the magnetic zone ( $-\pi/2 < k \leq \pi/2$ ,  $k_{\perp} = 0, \pi$ ). The operators  $b_{\mathbf{k},\sigma}^c$  and  $b_{\mathbf{k},\sigma}^v$  are given by the following transformation<sup>18</sup>:

$$b_{\mathbf{k},\sigma}^c = u_{\mathbf{k}} c_{\mathbf{k},\sigma} \mp v_{\mathbf{k}} c_{\mathbf{k}+\mathbf{Q},\sigma}, \quad (6)$$

$$b_{\mathbf{k},\sigma}^v = v_{\mathbf{k}} c_{\mathbf{k},\sigma} \pm u_{\mathbf{k}} c_{\mathbf{k}+\mathbf{Q},\sigma}, \quad (7)$$

where  $\mathbf{Q} = (\pi, \pi)$ , the upper (lower) sign corresponds to  $\sigma = \uparrow$  ( $\sigma = \downarrow$ ), and

$$u_{\mathbf{k}} = \sqrt{\frac{1}{2}(1 + \varepsilon_{\mathbf{k}}/E_{\mathbf{k}})}, \quad (8)$$

$$v_{\mathbf{k}} = \sqrt{\frac{1}{2}(1 - \varepsilon_{\mathbf{k}}/E_{\mathbf{k}})}, \quad (9)$$

$$E_{\mathbf{k}} = \sqrt{\Delta^2 + \varepsilon_{\mathbf{k}}^2}. \quad (10)$$

Here  $\varepsilon_{\mathbf{k}}$  is the free particle energy ( $U = 0$ ) defined in Eq. (2). The spin-density-wave gap,  $\Delta$ , is self-consistently determined by the equation

$$\frac{1}{U} = \frac{1}{2L} \sum_{\mathbf{k}}' \frac{1}{E_{\mathbf{k}}}. \quad (11)$$

The band structure of the AFHF Hamiltonian is given by  $\pm E_{\mathbf{k}} = \pm \sqrt{\Delta^2 + \varepsilon_{\mathbf{k}}^2}$  in the magnetic Brillouin zone. The SDW gap  $\Delta$ , calculated by solving Eq. (11) self-consistently, is shown as a function of  $t_{\perp}/t$  for  $U/t = 2, 4$ , and 8 in Fig. 5. The transition from a two-band metal to a band insulator in the  $U = 0$  system occurs at  $t_{\perp}/t = t_{\perp c} = 2.0$ . As  $U$  is turned on for  $t < t_{\perp c}$  in the AFHF, a gap develops in both the bonding and antibonding bands, leading to a four-band insulator. If  $t_{\perp}$  is then increased,  $\Delta$  will go to zero at approximately the noninteracting ( $U = 0$ )  $t_{\perp c}/t = 2.0$ , as seen for  $U/t = 2$  in Fig. 5, leading to a transition from a four-band to a two-band insulator. For large  $U$  and small  $t_{\perp}$ ,  $\Delta \approx U/2$ , as seen for  $U/t = 8$  in Fig. 5, so the Coulomb splitting of the bands will dominate over  $U = 0$  band structure effects. In this case, the gap will go to zero, i.e. the system will undergo a transition to a band insulator only when the band structure splitting  $2t_{\perp}$ , is of the order of the Coulomb splitting, so that  $t_{\perp c} \approx \Delta \approx U/2$ .

The spectral weight within the AFHF approximation is

$$A(\mathbf{k}, \omega) = u_{\mathbf{k}}^2 \delta(\omega - E_{\mathbf{k}}) + v_{\mathbf{k}}^2 \delta(\omega + E_{\mathbf{k}}). \quad (12)$$

We show the spectral weight  $A(\mathbf{k}, \omega)$  from AFHF for the same parameters as in Fig. 1 and Fig. 3 in Fig. 6(a) for

$t_{\perp}/t = 2.0$  and Fig. 6(b) for  $t_{\perp}/t = 0.5$ . The band splitting  $2\Delta \approx U$  in both cases, as can also be seen in Fig. 5. Since both the bonding and antibonding bands are split by this gap, there are two peaks in  $A(\mathbf{k}, \omega)$  as a function of  $\omega$  for each  $\mathbf{k}$ , leading to a four-band insulator for both values of  $t_{\perp}/t$ . Since the band splitting is set by  $U$  rather than  $2t_{\perp}$ , the spectral weight is almost evenly distributed between two coherent bands for both  $t_{\perp}/t = 2.0$  and  $t_{\perp}/t = 0.5$ . Therefore, for  $t_{\perp}/t = 2.0$ , as can be seen by comparing the QMC results in Fig. 1 with Fig. 6(a), the AFHF spectral weight distribution for  $t_{\perp}/t = 2.0$  is completely wrong, with too much weight in the upper,  $\omega > 0$ , band for  $k_{\perp} = 0$  and the  $\omega < 0$  band for  $k_{\perp} = \pi$ . While the average positions of the AFHF bands, shown as thick solid lines in Fig. 1(c), are approximately the same as those of the QMC bands, the band widths are too small by approximately a factor of two. For  $t_{\perp}/t = 2.0$  and  $U/t = 8$ , then, the AFHF calculation results in a four-band insulator in which there is long-range antiferromagnetic order, while the QMC results show that the system is a two-band insulator, with only very short range antiferromagnetic correlations. While the AFHF picture does produce a two-band insulator for  $t_{\perp}/t \gtrsim 4.5$ , the physical picture of the transition to this phase is quite different (see section C).

For  $t_{\perp}/t = 0.5$ , as seen in Fig. 3 and Fig. 6(b), AFHF gives two dispersive bands in the  $k_{\perp} = 0$  branch of width of order  $J \sim 4t^2/U$ , similar to the coherent bands seen in the QMC data. However, in the AFHF, the single particle gap is somewhat too large, the weight distribution extends too far towards  $k = \pi$  and too far towards  $k = 0$  for the photoemission and inverse photoemission parts of the spectrum, respectively, and the broad incoherent background is not present. We have also carried out mean-field slave boson calculations<sup>20</sup> in order to try to improve on the AFHF picture. These calculations give a gap about 15% smaller than AFHF, and a bandwidth about 3% smaller, but do not qualitatively improve on the AFHF calculations. The same holds for  $t_{\perp}/t = 1.0$ , where the AFHF describes approximately the coherent part of the spectrum and also produces a too large single particle gap and a slightly different spectral weight distribution. Therefore, for  $t_{\perp}/t = 0.5$  and for  $t_{\perp}/t = 1.0$ , AFHF would give a reasonable description of the dispersion and general spectral weight distribution of the coherent spin-wave bands, if the gap were phenomenologically adjusted to a smaller value, but fails to even qualitatively describe the spectral weight distribution for  $t_{\perp}/t = 2.0$ .

### C. Local Rung Approximation

For very large  $t_{\perp}$ , a better starting point is the limit of weak interaction between the rungs. In this limit, we split the Hamiltonian of Eq. (1) into  $H = H_0 + H_I$  with

$$H_0 = -t_{\perp} \sum_{i,\sigma} (c_{i,1\sigma}^{\dagger} c_{i,2\sigma} + h.c.) + U \sum_{i\lambda} n_{i,\lambda\uparrow} n_{i,\lambda\downarrow},$$

$$H_I = -t \sum_{i,\lambda\sigma} (c_{i,\lambda\sigma}^\dagger c_{i+1,\lambda\sigma} + h.c.), \quad (13)$$

where  $H_0$  denotes the non-interacting rung limit. The ground state of  $H_0$  is a product of individual rung eigenstates. Accordingly, we first diagonalize the Hubbard Hamiltonian on the two sites making up the rung in order to find the rung eigenstates. A schematic diagram of the exact eigenstates for a single rung is shown in Fig. 7. The ground state for the half-filled rung  $i$  (two particles per rung) is a spin singlet state with  $k_\perp = 0$  and energy  $E_0/L = E_0^{\text{rung}} = (U - \sqrt{U^2 + 16t_\perp^2})/2$  denoted by  $|S_i\rangle$ . For large values of  $U$ , the energy of this two-site state is given by the exchange coupling  $-J_\perp \sim -4t_\perp^2/U$ . Note that  $|S_i\rangle$  contains terms which have double occupied sites as well as the usual singlet construction  $(|\uparrow, \downarrow\rangle - |\downarrow, \uparrow\rangle)/\sqrt{2}$ .

We can then form an approximation to the ground state for the half-filled system by taking a state which is just a product of the rung states,

$$|\psi_0\rangle = |S_1\rangle|S_2\rangle\dots|S_L\rangle. \quad (14)$$

For  $t_\perp/t = 2.0$ , the binding energy of a singlet formed on a rung is about four times lower than the energy of a singlet between neighboring sites along a chain, and therefore we expect  $|\psi_0\rangle$  to be a good approximation to the exact ground state.

In order to obtain the  $\omega < 0$  spectral weight for the half-filled system, we need to calculate the matrix element of  $c_{\mathbf{k},\sigma}$  given in Eq. (3). In other words, we need matrix elements between a half-filled state and a state with one particle removed. We form the approximate one hole state by replacing one bond singlet state at rung  $\ell$ ,  $|S_\ell\rangle$ , with the lowest energy one-particle state, the one with bonding ( $k_\perp = 0$ ) symmetry,  $|B_{\ell\uparrow}\rangle$  (We remove a spin down electron for definiteness.) and define

$$|\ell\rangle = |S_1\rangle|S_2\rangle\dots|B_{\ell\uparrow}\rangle\dots|S_L\rangle. \quad (15)$$

We delocalize the single-particle state with a plane wave ansatz by constructing the state<sup>6,21</sup>

$$|\psi_1(k)\rangle = L^{-1/2} \sum_{\ell=1}^L e^{ik\ell} |\ell\rangle. \quad (16)$$

Trivially, this state is an exact eigenstate of  $H_0$ . We will take this state as the ground state for the system with one hole with momentum  $\mathbf{k} = (k, 0)$ . The spectral weight  $A(\mathbf{k}, \omega)$  at zero temperature ( $\beta \rightarrow \infty$ ) is then approximated by using only the two states  $|\psi_0\rangle$  and  $|\psi_1(k)\rangle$  in Eq. (3). For  $k_\perp = 0$ , the energy dispersion  $\omega(k)$  of  $A(\mathbf{k}, \omega)$  for  $\omega < 0$  is given by

$$\begin{aligned} \omega(k) &= \langle \psi_0 | H | \psi_0 \rangle - \langle \psi_1(k) | H | \psi_1(k) \rangle - \mu \\ &= -\frac{1}{2} \sqrt{U^2 + 16t_\perp^2} + t_\perp - tA \cos k, \end{aligned} \quad (17)$$

with  $A = (1 + E_2/2t_\perp)/(1 + E_2^2/4t_\perp^2)$ ,  $E_2 = (U + \sqrt{U^2 + 16t_\perp^2})/2$ , and the corresponding spectral weight by  $|\langle \psi_1(k) | c_{k,\downarrow} | \psi_0 \rangle|^2$ . The dispersion given by Eq. (17) for  $U/t = 8$  and  $t_\perp/t = 2.0$  is plotted in Fig. 1(c) and the spectral weight for  $k_\perp = 0$  is shown in Fig. 8. One can see that the position of the peak of the  $\omega < 0$  LRA band, denoted LRA1 in Fig. 1(c), lays almost exactly on the QMC data. However, the position and the dispersion of the  $\omega > 0$  band, which were obtained in the same way as for  $\omega < 0$ , are not exactly matched by the LRA1 calculation. While this band is not very important in the sense that it contains very little spectral weight, we can understand how to improve the LRA1 calculation by considering the states of a four site cluster.

In order to generate the inverse photoemission spectrum, we need to calculate matrix elements between the half-filled state and a state with one *additional* particle. From Fig. 7, we see that a rung state with three particles and  $k_\perp = 0$  has approximately twice the excitation energy of the  $k_\perp = 0$  one-particle state which is relevant for the photoemission part of the spectrum. (Recall that due to the particle-hole symmetry at half-filling, this state will map to one in the inverse photoemission part of spectrum for  $k = \pi$ ; one can see this symmetry in Fig. 7.) Since the relevant three-particle single rung state is high in energy, configurations involving intrachain effects might also be important. We include the effect of such configurations by replacing two rung singlet states by the lowest energy state of five particles on four sites in the bonding channel. We can then form a delocalized plane wave state from this state as in Eq. (16). The results of this calculation are labeled as LRA2 in Fig. 1(c). The location and width of the  $k_\perp = 0$  inverse photoemission band are more closely fit than by the LRA1 calculation. In Fig. 8 the spectral weight distribution of the LRA1 calculation for the photoemission part of the spectrum ( $\omega < 0$ ) and the distribution of the LRA2 calculation for the inverse photoemission part ( $\omega > 0$ ) is plotted. The result is in good accordance with the QMC data in Fig. 1(a).

### III. SPIN AND CHARGE DYNAMIC CORRELATION FUNCTIONS

In order to determine the nature of the low lying excitations, we also consider the spin and charge susceptibilities  $\chi_{s,c}(\mathbf{q}, \omega)$  which, in a Lehmann representation, are defined as

$$\begin{aligned} \chi_{s,c}(\mathbf{q}, \omega) &= \frac{i}{Z} \sum_{l,l'} e^{-\beta E_l} (1 - e^{-\beta \omega}) |\langle l | O_{s,c}(\mathbf{q}) | l' \rangle|^2 \\ &\quad \cdot \delta(\omega - (E_{l'} - E_l)), \end{aligned} \quad (18)$$

with  $O_s(\mathbf{q}) = \sum_{\mathbf{p}} (c_{\mathbf{p}+\mathbf{q},\uparrow}^\dagger c_{\mathbf{p},\uparrow} - c_{\mathbf{p}+\mathbf{q},\downarrow}^\dagger c_{\mathbf{p},\downarrow})$  and  $O_c(\mathbf{q}) = \sum_{\mathbf{p},\sigma} c_{\mathbf{p}+\mathbf{q},\sigma}^\dagger c_{\mathbf{p},\sigma}$ . We calculate the two-particle dynamic

response from the two-particle imaginary time Green's function, as in Eq. (4) and use the Maximum Entropy method described above for the analytical continuation of  $\chi_{s,c}(\mathbf{q}, \omega)$  to real frequencies.

In Fig. 9 we show the dynamical spin-spin correlation function  $\chi_{s,c}(\mathbf{q}, \omega)$  for  $t_{\perp}/t = 2.0$  and  $t_{\perp}/t = 1.0$ . For  $t_{\perp}/t = 2.0$ , the  $q_{\perp} = 0$  component [Fig. 9(a)] has a broad, lightly weighted structure centered approximately at  $\omega = 3t$ , with the spectral weight vanishing for small  $q$ . For  $q_{\perp} = \pi$  [Fig. 9(b)], there is a coherent, dispersive band with a width set by  $J \approx 4t^2/U = 0.5t$ , a minimum at  $q = \pi$  and a maximum at  $q = 0$ . The minimum spin gap is approximately  $0.8t$ , which agrees well with the value we obtain using Projector Quantum Monte Carlo, indicated by the dashed line on the plot. The spectral weight is most heavily concentrated around  $q = \pi$ .

The dynamic spin response at half-filling measures the response of the system to spin triplet excitations. Since here  $t_{\perp}$  is large, we consider the effect of triplet excitations on product rung states of the type considered in Eq. (14), in the LRA calculation. A triplet excitation will change the total spin of the state from  $S = 0$  to  $S = 1$ . Referring to Fig. 7, the only triplet excited state on a single rung has momentum  $\pi$  (corresponding to odd parity under chain interchange) leading to a change in momentum  $q_{\perp} = \pi$  for the triplet excitation. The size of this triplet excitation  $\Delta E_s^{\text{rung}}$  is marked on Fig. 9(b) by the solid line. This local triplet excited state can be moved to a near neighbor rung by a process which is second order in  $H_I$ . The local triplet excited states can then be delocalized into a Bloch wave as in Eq. (15) and Eq. (16). For large  $U$ , one then obtains a dispersion relation of the form  $\Delta E_s^{\text{rung}} + J \cos q$ , where  $J \sim 4t^2/U$ , a form similar to that obtained in Ref. 5 for the two chain Heisenberg model. The coherent band in Fig. 9(b) does have a minimum at  $q = \pi$ , and has approximately this form.

Within the LRA picture, it is also possible to excite a  $q_{\perp} = 0$  (even under chain interchange) triplet excitation via a ‘‘two-magnon’’ process, as discussed in Ref. 5. This corresponds to making two local triplet excitations on rungs in the non-interacting rung picture, and would lead to an excitation energy whose scale, in the Heisenberg limit, is set by  $\omega \sim 2J_{\perp}$  rather than  $\omega \sim J_{\perp}$ . The overall position of the lightly weighted band seen for  $q_{\perp} = 0$  in Fig. 9(a) is consistent with this two-magnon band, although the band is too lightly weighted and our resolution too low to extract a dispersion relation.

For the physical relevant isotropic case ( $t_{\perp}/t = 1.0$ ), shown in Fig. 9(c) and (d), the spin response looks quite different. (Because the  $t_{\perp}/t = 0.5$  results are qualitatively similar to the  $t_{\perp}/t = 1.0$  results, we show only the isotropic ( $t_{\perp}/t = 1.0$ ) case here.) In Fig. 9(c) and (d), there are dispersive bands in both the  $q_{\perp} = 0$  and  $q_{\perp} = \pi$  branches, with the position of the peak going to a finite minimum at  $\mathbf{q} = (0, \pi)$  and  $\mathbf{q} = (\pi, 0)$ , and appears to vanish as  $\mathbf{q} \rightarrow (\pi, \pi)$ . However, as shown in Fig. 4, the correlation length is 4.3 lattice spacings in this regime,

and there should be a spin gap. Using DMRG calculations on lattices of  $2 \times 8$  to  $2 \times 32$  sites<sup>8</sup>, we estimate the spin gap to be of order  $0.12t$ . Due to finite size effects and finite resolution in the analytic continuation, this gap is too small to resolve in Fig. 9(d). Near  $\mathbf{q} = (0, 0)$  [Fig. 9(c)], the dispersion of the peak is hard to discern because there is very little spectral weight. This lack of spectral weight at  $\mathbf{q} = (0, 0)$  is present in all the dynamic charge and spin correlations and is due to a selection rule that comes about because  $O_{s,c}(\mathbf{q} = \mathbf{0})$  in Eq. (18) commutes with the Hamiltonian, leading to a vanishing of the matrix element of  $O_{s,c}(\mathbf{q})$  as  $\mathbf{q} \rightarrow \mathbf{0}$ . Therefore, the system has relatively long-range spin order in this regime and, to within the resolution of our calculations, shows the characteristics of an ordered state with gapless excitations. Thus it is interesting to compare the QMC spectra to the results of spin-wave theory calculations.

In order to extract the low-lying spin excitations using spin-wave theory it is necessary to consider the RPA transverse spin susceptibility  $\chi_{\text{RPA}}^{+-}(\mathbf{k}, \mathbf{k}', \omega)$ . It is obtained by applying the random-phase approximation to the response function  $\chi_0^{+-}(\mathbf{k}, \mathbf{k}', \omega)$ , which is calculated directly in real time using the AFHF ground state  $|\Omega\rangle$ , calculated in section II B:

$$\chi_0^{+-}(\mathbf{q}, \mathbf{q}', t) = \frac{i}{4L} \langle \Omega | T S_{\mathbf{q}}^{+}(t) S_{-\mathbf{q}'}^{-}(0) | \Omega \rangle, \quad (19)$$

with  $S^{\pm} = S_x \pm iS_y$ . Due to the broken spin rotational symmetry of  $|\Omega\rangle$ ,  $\chi_{\text{RPA}}^{+-}(\mathbf{q}, \mathbf{q}', \omega)$  contains a gapless mode, as predicted by the Goldstone theorem. Following the procedure of Schrieffer et al.<sup>18</sup>, one obtains:

$$\chi_{\text{RPA}}^{+-}(\mathbf{q}, \mathbf{q}', \omega) = \sum_{\mathbf{p}} \chi_0^{+-}(\mathbf{q}, \mathbf{p}, \omega) [1 - U \chi_0^{+-}(\mathbf{p}, \mathbf{q}', \omega)]^{-1}, \quad (20)$$

where  $[1 - U \chi_0^{+-}(\mathbf{p}, \mathbf{q}', \omega)]^{-1}$  is a matrix inverse of a  $2 \times 2$  matrix in  $\mathbf{q}$ -space and

$$\chi_0^{+-}(\mathbf{q}, \mathbf{q}', \omega) = \delta(\mathbf{q} - \mathbf{q}') \chi_0^{+-}(\mathbf{q}, \omega) + \delta(\mathbf{q} - \mathbf{q}' + \mathbf{Q}) \chi_Q^{+-}(\mathbf{q}, \omega), \quad (21)$$

with  $\chi_0^{+-}(\mathbf{q}, \omega)$  and  $\chi_Q^{+-}(\mathbf{q}, \omega)$  given by the usual ‘‘bubble’’ diagrams and printed in detail in Ref. 16 [up to a misprint of a factor of 2 in  $\chi_Q^{+-}(\mathbf{q}, \omega)$ ]. The dispersion of  $\chi_{\text{RPA}}^{+-}(\mathbf{q}, \mathbf{q}, \omega)$  is indicated as a solid line in Fig. 9(c) and 9(d). The RPA spin-wave dispersion goes to zero at  $\mathbf{q} = (0, 0)$  and  $\mathbf{q} = (\pi, \pi)$ , and goes to a finite minimum at  $\mathbf{q} = (0, \pi)$  and  $\mathbf{q} = (\pi, 0)$ , consistent with the QMC data. The spin-wave velocity, the width of the bands, and the gaps at  $\mathbf{q} = (0, \pi)$  and  $\mathbf{q} = (\pi, 0)$  are also in reasonable agreement with the QMC data.

The QMC results for the dynamic charge correlation function are shown in Fig. 10 for  $t_{\perp}/t = 2.0$  and  $t_{\perp}/t = 1.0$ . For  $t_{\perp}/t = 2.0$ , almost all of the spectral weight is in the  $q_{\perp} = \pi$  component, so we do not show the  $q_{\perp} = 0$  component. There exist two important features:

one is a heavily weighted, relatively flat band at  $\omega \sim 10t$  with heaviest weight near  $q = 0$ . This band becomes somewhat incoherent as  $q$  increases. The second is a flat, dispersive, less heavily weighted band with a minimum of order  $5t$  near  $q = \pi$ . The spectral weight in this band extends from about  $q = \pi/4$  to  $q = \pi$ , and the size of the charge gap is set by this lightly weighted lower band.

In the large  $t_\perp$  limit, one can understand the structure of the charge response from the LRA picture described in section II C. In the single rung picture, a charge excitation will occur through a transition to an excited state conserving the number of particles on the rung and the total spin; in other words, the important transition will be in the middle column of Fig. 7, from the low-lying  $S = 0$  state to the higher  $S = 0$  states. There are two possible charge excited states on the rung, one with momentum  $k_\perp = 0$  (even parity) and one with momentum  $k_\perp = \pi$  (odd parity). In a single rung picture, an optical transition from the  $k_\perp = 0$  ground state to a  $k_\perp = 0$  excited state is forbidden because the  $q_\perp = 0$  density operator  $O_c(0)$  commutes with the Hamiltonian. This selection rule forbidding a  $q_\perp = 0$  optical transition remains present when the rung charge excited states are constructed as in Eq. (15) and delocalized in a state like that in Eq. (16). This is why there is almost no spectral weight in the  $q_\perp = 0$  portion of the charge response for  $t_\perp/t = 2.0$ . Of course, the system is not exactly in a LRA state, so there will be some higher order processes that will introduce a very small amount of spectral weight into the  $q_\perp = 0$  branch. The energy of the  $q_\perp = \pi$  single rung transition, indicated by a solid line on the Fig. 10(a), gives an excitation energy that agrees well with energy of the heavily weighted region at  $q = 0$ .

In order to qualitatively understand the origin of the dispersion of the charge response, one can consider the possible particle-hole excitations within the one-particle band structure given by  $A(\mathbf{k}, \omega)$  in Fig. 1. There will be significant amplitude in the two-particle charge response when there is significant amplitude for a transition at a particular  $\mathbf{q} = (q, q_\perp)$  and  $\omega$  for a particle-hole excitation built up from the one-particle spectral weight. For example, to understand the heavily weighted amplitude at  $\mathbf{q} = (0, \pi)$ , one has to integrate over all transitions from the photoemission band in Fig. 1(a) to the inverse photoemission band in Fig. 1(b) which transfer this momentum. Since the single-particle bands are sharp and parallel, one should obtain a single well-defined peak for  $\mathbf{q} = (0, \pi)$ , which we see in Fig. 10(a) by considering excitations between the  $\omega < 0, k_\perp = 0$  band, and the  $\omega > 0, k_\perp = \pi$  band. In addition, the transition at  $\mathbf{q} = (0, \pi)$  has odd parity between the chains, and is thus allowed by the selection rules for the density operator as  $q \rightarrow 0$ . As the parallel component  $q$  is increased, one can see that there will be a continuum of excitation energies which gets wider as  $q$  increases. The minimum excitation energy (position of the lower band) from this construction is shown in Fig. 10(a) by the line with solid dots. However, the excitation energy obtained is consistently

smaller than the energy of the lowest heavily weighted band from QMC. Using the single particle bands to construct the two-particle excitations is equivalent to calculating the charge response using the lowest order ‘‘bubble’’ diagram, but with exact single-particle propagators, neglecting all particle-hole interactions. The particle-hole interactions on the rung, which are included in the rung eigenenergies, thus raise the charge excitation energy by a substantial amount<sup>22</sup>.

For  $t_\perp/t = 1.0$ , the charge response looks quite different. As shown in Fig. 10(b) and (c), there is substantial spectral weight for both  $q_\perp = 0$  and  $q_\perp = \pi$ . For  $\mathbf{q} \rightarrow (0, 0)$ , the density operator has even parity, causing the matrix element and thus the spectral weight to vanish, whereas at  $\mathbf{q} \rightarrow (0, \pi)$ , the density operator has odd parity so that optical transitions are allowed and there is spectral weight. In both channels, the size of the charge gap is approximately  $4t$ , and there is a broad structure of width  $\sim 7t$ . For  $q_\perp = 0$ , most of the spectral weight occurs as a dispersive peak whose energy increases with increasing  $q$ , whereas for  $q_\perp = \pi$  two peaks seem to contribute to the spectral weight distribution. The peaks are not well-defined enough over a range of  $q$  to extract a dispersion, but the upper peak is heavily weighted near  $q = \pi$ , at  $\omega \approx 9t$ .

We can qualitatively understand the broad incoherent structure of the charge response by considering particle-hole excitation in the single particle  $A(\mathbf{k}, \omega)$  in Fig. 2. There are four dispersive bands and a broad background, so there should be weight in both the  $q_\perp = 0$  and  $q_\perp = \pi$  branches of the charge response, and broad structure above a minimum excitation energy, which we see in Fig. 10(c) and (d). From the single particle bands in Fig. 3, one can estimate the minimum particle-hole excitation energy to be  $\sim 4t$ . In Fig. 10(c) and (d), the spectral weight near this minimum excitation energy is suppressed due to the particle-hole vertex. We have also carried out a calculation of charge response  $\chi_{\text{RPA}}^{00}(\mathbf{q}, \mathbf{q}', \omega)$  within the antiferromagnetic RPA approximation described above, using the SDW dispersion in Eq. (10), and also find a relatively broad structure above the charge gap for both  $q_\perp = 0$  and  $q_\perp = \pi$ . We plot the minimum excitation energy of  $\chi_{\text{RPA}}^{00}(\mathbf{q}, \mathbf{q}', \omega)$  in Fig. 10(b) and (c) as lines with solid dots. This line is located in the middle of the broad band in both plots.

The spin and charge response functions for  $t_\perp/t = 0.5$  show the same general features as in the isotropic ( $t_\perp/t = 1.0$ ) case and are therefore not shown here. The spin susceptibility  $\chi_s(\mathbf{q}, \omega)$  is also qualitatively identical to the RPA result  $\chi_{\text{RPA}}^{+-}(\mathbf{q}, \mathbf{q}, \omega)$  with a smaller spin velocity than in the  $t_\perp/t = 1.0$  case. The charge susceptibility  $\chi_c(\mathbf{q}, \omega)$  shows a clear dispersive band centered around the low-lying RPA excitations in the  $q_\perp = 0$  channel, whose energy increases with increasing  $q$ . In the  $q_\perp = \pi$  channel, there is a broad structure of width  $\sim 8t$  with again two peaks in the spectral weight distribution.

## IV. CONCLUSION

In summary, the single and two-particle dynamical properties of the two chain Hubbard model at half-filling can be understood by starting from two limits: the limit of non-interacting rungs treated exactly, which gives a good starting point for the large  $t_{\perp}$  case for which the spin-spin correlation length along the chains is less than a lattice spacing, and the limit of an antiferromagnetically ordered state, which gives a good starting point for the small  $t_{\perp}$  case when the spin-spin correlation length is large. The dynamical properties in the two regimes look quite different. For the large  $t_{\perp}$  regime, the remnants of the level transitions of the two site system representing a single rung, suitably broadened into bands, can explain the major features of the single-particle, spin and charge responses. In the small  $t_{\perp}$  case, calculations based on an antiferromagnetically ordered starting point, such as antiferromagnetic Hartree-Fock theory and spin-wave theory give a good qualitative picture of the coherent spin-wave part of the single particle spectral weight and of the two-particle spin dynamic correlation function. In addition, there is a broad incoherent band in the single particle spectral weight similar to that found in recent numerical work on the 1D and 2D systems.

We also have shown the single particle spectral weight and the spin and charge response functions for the physical relevant, isotropic case ( $t_{\perp}/t = 1.0$ ). The results are qualitatively similar to these in the small  $t_{\perp}$  region and can therefore be understood from an antiferromagnetic Hartree-Fock or spin-wave theory picture. The real ladder compounds have approximately the same coupling strength parallel to and perpendicular to the chains, and it will therefore be interesting to compare these isotropic  $t_{\perp}/t = 1.0$  results with future experiments.

## ACKNOWLEDGMENTS

We would like to thank R. Preuss, A. Muramatsu, and W. Ziegler for helpful discussions. H.E., W.H., and R.M.N. are grateful to the Bavarian "FORSUPRA" program on high  $T_c$  research and the DFG under Grant No. Ha 1537/12-1 for financial support. D.P. acknowledges support from the EEC Human Capital and Mobility program under grant CHRX-CT93-0332, and D.J.S. from the NSF under Grant No. DMR 92-2507. The calculations were performed on Cray YMP's at the HLRZ in Jülich and at the LRZ München.

- 
- <sup>1</sup> Z. Hiroi, M. Azuma, M. Takano, and Y. Bando, *J. Solid State Chem.*, **95**, 230 (1991).
  - <sup>2</sup> D.C. Johnston *et al.*, *Phys. Rev. B* **35**, 219 (1987).
  - <sup>3</sup> T.M. Rice, S. Gopalan, and M. Sigrist, *Europhys. Lett.* **23**, 445 (1993).
  - <sup>4</sup> Z. Hiroi, and M. Takano, *Nature* **377**, 41 (1995).
  - <sup>5</sup> E. Dagotto, J. Riera, and D.J. Scalapino, *Phys. Rev. B* **45**, 5744 (1992).
  - <sup>6</sup> T. Barnes *et al.*, *Phys. Rev. B* **47**, 3196 (1993); T. Barnes and J. Riera, *Phys. Rev. B* **50**, 6817 (1994); R.S. Eccleston, T. Barnes, J. Brody, and J.W. Johnson, *Phys. Rev. Lett.* **73**, 2626 (1994).
  - <sup>7</sup> S.R. White, R.M. Noack, and D.J. Scalapino, *Phys. Rev. Lett.* **73**, 886 (1994).
  - <sup>8</sup> R.M. Noack, S.R. White, and D.J. Scalapino, *Phys. Rev. Lett.* **73**, 882 (1994); *Europhys. Lett.* **30** (3), 163 (1995).
  - <sup>9</sup> H. Tsunetsugu, M. Troyer, and T.M. Rice, *Phys. Rev. B* **49**, 16078 (1994).
  - <sup>10</sup> R.N. Silver, D.S. Sivia, and J.E. Gubernatis, *Phys. Rev. B* **41**, 2380 (1990), and references therein.
  - <sup>11</sup> L. Balents, and M.P.A. Fisher, to be published, *cond-mat/9504082*.
  - <sup>12</sup> R. Preuss, A. Muramatsu, W. von der Linden, P. Dieterich, F.F. Assaad, and W. Hanke, *Phys. Rev. Lett.* **73**, 732 (1994).
  - <sup>13</sup> R. Preuss, A. Muramatsu, W. von der Linden, and W. Hanke, unpublished.
  - <sup>14</sup> R. Preuss, W. Hanke, and W. von der Linden, to be published, *cond-mat/9412089*.
  - <sup>15</sup> A. Moreo, S. Haas, A. Sandvik, and E. Dagotto, to be published, *cond-mat/9412107*.
  - <sup>16</sup> W. von der Linden, R. Preuss and W. Hanke, to be published, *cond-mat/9503098*.
  - <sup>17</sup> S.R. White, *Phys. Rev. B* **44**, 4670 (1991).
  - <sup>18</sup> J.R. Schrieffer, X.G. Wen, and S.C. Zhang, *Phys. Rev. B* **39**, 11663 (1989).
  - <sup>19</sup> A.P. Kampf and J.R. Schrieffer, *Phys. Rev. B* **42**, 7967 (1990).
  - <sup>20</sup> L. Lilly, A. Muramatsu, and W. Hanke, *Phys. Rev. Lett.* **65**, 1379 (1990), and references therein.
  - <sup>21</sup> I. Bose and S. Gayan, *Phys. Rev. B* **48**, 10653 (1993).
  - <sup>22</sup> W. Hanke, and L.J. Sham, *Phys. Rev. Lett.* **43**, 387 (1979); *Phys. Rev. B* **21**, 4656 (1980).



FIG. 1. QMC result for the spectral density function  $A(\mathbf{k}, \omega)$  for all possible values of  $\mathbf{k} = (k, k_\perp)$  on a  $2 \times 16$  system with  $U/t = 8$  and  $t_\perp/t = 2.0$  at an inverse temperature of  $\beta = 10/t$ . Parts (a) and (b) are three-dimensional plots on the  $\omega$ - $k$  plane for  $k_\perp = 0$  and  $k_\perp = \pi$ , respectively. Part (c) is a density plot for the  $k_\perp = 0$  branch with darker shading corresponding to higher spectral weight, and the points with error bars showing the position of the peaks. The thick solid line indicates the SDW result within AFHF at  $T = 0$ , the dashed line is the calculated local rung approximation (LRA) dispersion for local excitations on one rung (LRA1) and the long-dashed line shows the spectrum obtained by local excitations on a four-site cluster (LRA2).

FIG. 2. The single particle spectral weight  $A(\mathbf{k}, \omega)$  as in Fig. 1, with the same parameters except with an isotropic hopping,  $t_\perp/t = 1.0$ . In (c), the solid line is the SDW result calculated within AFHF.

FIG. 3. The single particle spectral weight  $A(\mathbf{k}, \omega)$  as in Fig. 1, with the same parameters except with  $t_\perp/t = 0.5$ . In (c), the solid line is the SDW result calculated within AFHF.

FIG. 4. The spin-spin correlation function  $S(r)$  for  $t_\perp = 2t$ ,  $t_\perp = t$  and  $t_\perp = 0.5t$  calculated on a  $2 \times 32$  lattice with  $U/t = 8$  and open boundary conditions using the DMRG. The solid, dotted and dashed lines are asymptotic fits to the data using the simple exponential form  $A \exp(-r/\xi)$ .

FIG. 5. The SDW gap calculated within the AFHF approximation at  $T = 0$ , as a function of  $t_\perp/t$  on a  $2 \times 100$  grid for  $U/t = 2, 4, 8$ .

FIG. 6. Spectral weight calculated within the AFHF approximation for (a)  $t_\perp/t = 2.0$  and (b)  $t_\perp/t = 0.5$  with  $U/t = 8$ , shown for  $k_\perp = 0$  and  $k_\perp = \pi$ .

FIG. 7. Exact eigenstates for a two-site system representing a disconnected rung, with  $U = 8$  and  $t_\perp = 2.0$ . The horizontal axis is the number of particles and the vertical axis shows the total energy  $\langle (H - \mu N) \rangle$ , where the chemical potential  $\mu = U/2$  at half-filling. Each level is labeled with the total spin  $S$  and momentum  $k_\perp$ .

FIG. 8. Spectral weight using LRA1 calculation for the  $\omega < 0$  and the LRA2 calculation for the  $\omega > 0$  parts of the spectrum for  $k_\perp = 0$ . Here  $t_\perp/t = 2.0$  and  $U/t = 8$ .

FIG. 9. Dynamic spin response function  $\chi_s(\mathbf{q}, \omega)$  for (a)  $t_\perp/t = 2.0$ ,  $q_\perp = 0$ , (b)  $t_\perp/t = 2.0$ ,  $q_\perp = \pi$ , (c)  $t_\perp/t = 1.0$ ,  $q_\perp = 0$ , and (d)  $t_\perp/t = 1.0$ ,  $q_\perp = \pi$ . Again,  $U/t = 8$  on a  $2 \times 16$  lattice. The weight of sizable structures is represented by the strength of shading in the shaded regions and the position of the maxima by the points with error bars. In (b), the solid line indicates the spin gap  $\Delta E_S^{\text{rung}}$  of the two-site system and the dashed line the spin gap  $\Delta E_S$  for the  $2 \times 16$  ladder at  $T = 0$ , calculated with a projector QMC algorithm. In (c) and (d), the solid lines are  $\chi_{\text{RPA}}^{\pm}(\mathbf{q}, \mathbf{q}, \omega)$  calculated using the SDW approximation given by Eq. (19).

FIG. 10. The dynamic charge response function  $\chi_c(\mathbf{q}, \omega)$  for the same parameters as in Fig. 7. In (a),  $t_\perp/t = 2.0$  and  $q_\perp = \pi$ , the solid line represents the charge excitation energy on a single rung  $\Delta E_C^{\text{rung}}$ , and the line with solid dots represents the minimum excitation energy constructed from the single particle spectral weight in Fig. 1. In (b) and (c),  $t_\perp/t = 1.0$ , and  $q_\perp = 0$  and  $\pi$ , respectively. The lines with solid dots represent the minimum excitation energy of the RPA charge susceptibility  $\chi_{\text{RPA}}^{00}(\mathbf{q}, \mathbf{q}, \omega)$  calculated with the method of Ref. 16.

# Dynamical Properties of Two Coupled Hubbard Chains at Half-filling

H. Endres<sup>a</sup>, R.M. Noack<sup>a</sup>, W. Hanke<sup>a</sup>, D. Poilblanc<sup>b</sup>, and D.J. Scalapino<sup>c</sup>

*a) Institut für Theoretische Physik, Universität Würzburg,  
Am Hubland, 97074 Würzburg, Germany*

*b) Université Paul Sabatier, Laboratoire de Physique Quantique,  
118 route de Narbonne, 31062 Toulouse, France*

*c) Department of Physics, University of California, Santa Barbara, CA 93106*

Using grand canonical Quantum Monte Carlo (QMC) simulations combined with Maximum Entropy analytic continuation, as well as analytical methods, we examine the one- and two-particle dynamical properties of the Hubbard model on two coupled chains at half-filling. The one-particle spectral weight function,  $A(\mathbf{k}, \omega)$ , undergoes a qualitative change with interchain hopping  $t_{\perp}$  associated with a transition from a four-band insulator to a two-band insulator. A simple analytical model based on the propagation of exact rung singlet states gives a good description of the features at large  $t_{\perp}$ . For smaller  $t_{\perp}$ ,  $A(\mathbf{k}, \omega)$  is similar to that of the one-dimensional model, with a coherent band of width the effective antiferromagnetic exchange  $J$  reasonably well-described by renormalized spin-wave theory. The coherent band rides on a broad background of width several times the parallel hopping integral  $t$ , an incoherent structure similar to that found in calculations on both the one- and two-dimensional models. We also present QMC results for the two-particle spin and charge excitation spectra, and relate their behavior to the rung singlet picture for large  $t_{\perp}$  and to the results of spin-wave theory for small  $t_{\perp}$ .

## I. INTRODUCTION

The compounds  $\text{SrCu}_2\text{O}_3$ <sup>1</sup> and  $(\text{VO})_2\text{P}_2\text{O}_7$ <sup>2</sup> consist of arrays of weakly interacting two-chain metal-oxide ladders. In  $\text{SrCu}_2\text{O}_3$ ,  $\text{CuO}_2$  ladders are coupled by a weak, frustrated, ferromagnetic coupling<sup>3</sup>, and in  $(\text{VO})_2\text{P}_2\text{O}_7$ ,  $\text{VO}_4$  ladders are well separated in the structure of the material. These materials have a half-filled conduction band, corresponding to one conduction electron per metal-oxide unit and are insulators with short-range antiferromagnetic correlations and a spin gap. Very recently Z. Hiroi and M. Takano<sup>4</sup> succeeded in doping the two-leg ladder compound  $\text{La}_{1-x}\text{Sr}_x\text{CuO}_{2.5}$ . They observe a fall in resistivity with doping, possibly to a metallic state, but no sign of superconductivity. The spin-gap found in half-filled  $\text{LaCuO}_{2.5}$  persists, but decreases with doping. In this publication we will address the half-filled situation only. The undoped materials have been described by a Heisenberg model on two coupled chains<sup>3,5-7</sup>, which explains a number of experimentally observed magnetic properties of the materials, including the size of the spin gap, and the spectrum of the spin triplet excitations. The Hubbard model on two coupled chains, which at half-filling and in the limit of strong on-site Coulomb repulsion can be mapped onto the Heisenberg model, gives an itinerant electron picture of these systems<sup>8</sup> which includes charge as well as spin fluctuations. While the ground state and the low-energy properties of the two-chain Heisenberg and half-filled Hubbard model are becoming well understood, less is known about the finite frequency one- and two-particle response. The dynamic spin response of the Heisenberg model was studied in Ref. 5 and the single particle and spin response was examined for a  $t$ - $J$

model with two holes in Ref. 8 using analytic continuation of Lanczos exact diagonalization calculations on small clusters. The dynamic properties are important because they can be measured with a variety of experimental techniques. For example, the one-particle spectral weight can be probed by photoemission and inverse photoemission, the dynamic charge correlation function by optical response measurements, and the dynamic spin structure factor by inelastic neutron scattering.

Here we examine the dynamic one- and two-particle correlation functions of the two-chain Hubbard model at half-filling using Quantum Monte Carlo simulations analytically continued to real frequencies using a Maximum Entropy technique<sup>10</sup>. We study the dynamic response for large, intermediate, and small values of the perpendicular hopping  $t_{\perp}$ . This is interesting for two reasons: first, when the electron-electron interaction is turned off ( $U = 0$ ) in the two-chain system, there is a metal-insulator transition from a two-band metal to a band insulator due to the separation of the bonding and antibonding bands with increasing  $t_{\perp}$ . For the interacting ( $U \neq 0$ ) case, it is generally believed that the two-chain system is always insulating (see, for example, Ref. 11 for a discussion within a weak-coupling RG picture). The QMC simulations do find an insulator for all  $t_{\perp}$ , but also reveal a crossover from four-band insulating behavior for small  $t_{\perp}$  to two-band behavior for  $t_{\perp}/t \gtrsim 2$ . A similar crossover occurs for weak coupling ( $U \lesssim t$ ) within antiferromagnetic Hartree-Fock (AFHF) theory, as we shall discuss in section II B. One interesting and important result of this paper is that this four-band to two-band crossover scenario survives in the intermediate to large  $U$  regime in the system, despite the fact that the

many-body physics for  $t_{\perp} \gtrsim t$  is not even qualitatively reproduced in the AFHF approximation. No such crossover is present as a function of  $J_{\perp}/J$  in the Heisenberg model, because the mapping to the Heisenberg model breaks down when  $J_{\perp} \sim 4t_{\perp}^2/U$  is of the order of  $t_{\perp}$ . In other words, the effect of the electronic band structure is not present in the Heisenberg model. As we shall see, this crossover can also be described in terms of the crossover from a localized rung picture, in which localized excitations form a Bloch state along the chains for large  $t_{\perp}$ , to a picture with longer range antiferromagnetic correlations with many features that can be qualitatively described by AFHF spin-wave theory for small  $t_{\perp}$ .

Secondly, in the small to intermediate  $t_{\perp}$  regime, this system displays features of the single-particle spectral weight  $A(\mathbf{k}, \omega)$  seen in recent numerical treatments of both the 1D<sup>12,13</sup> and 2D<sup>14,15</sup> Hubbard model. We find two features also generic to the 1D and 2D systems: a dispersive band whose width is of the order of the effective exchange interaction  $J \sim 4t^2/U$  and an incoherent background of width several times the parallel hopping integral  $t$ . For the one and two chain systems, but not the 2D system, the dispersive band is well described by renormalized spin-wave-theory.

We consider the single band Hubbard model on two coupled chains of length  $L$ :

$$H = -t \sum_{i,\lambda\sigma} (c_{i,\lambda\sigma}^{\dagger} c_{i+1,\lambda\sigma} + h.c.) - t_{\perp} \sum_{i,\sigma} (c_{i,1\sigma}^{\dagger} c_{i,2\sigma} + h.c.) + U \sum_{i\lambda} n_{i,\lambda\uparrow} n_{i,\lambda\downarrow}. \quad (1)$$

Here  $c_{i,\lambda\sigma}^{\dagger}$  and  $c_{i,\lambda\sigma}$  create and annihilate electrons on rung  $i$  and chain  $\lambda$  with spin  $\sigma$ , respectively, the hopping integral parallel to the chains is  $t$ , the hopping between the chains  $t_{\perp}$ , and  $U$  is an on-site Coulomb interaction. We use periodic boundary conditions parallel to and open boundary conditions perpendicular to the chains.

The non-interacting,  $U = 0$ , Hamiltonian can be diagonalized by writing the hopping term in terms of bonding and antibonding states on a rung and Fourier-transforming parallel to the chains. The energy is then given by

$$\varepsilon_{\mathbf{k}} = -(2t \cos k + t_{\perp} \cos k_{\perp}) \quad (2)$$

with  $\mathbf{k} = (k, k_{\perp})$ , where  $k_{\perp} = 0$  and  $k_{\perp} = \pi$  corresponds to the energy of the bonding and antibonding band, respectively, and  $k$  is the momentum along the chains. Both bands will be occupied when  $t_{\perp} < t_{\perp c}$ , whereas when  $t_{\perp} > t_{\perp c}$ , only the bonding band will be occupied. Here  $t_{\perp c}/t \equiv 1 - \cos \pi \langle n \rangle$  and  $\langle n \rangle \equiv \langle \sum_{\sigma} c_{i,\lambda,\sigma}^{\dagger} c_{i,\lambda,\sigma} \rangle$ . For half-filling  $t_{\perp c}/t = 2$ , and the system is a two-band metal for  $t_{\perp}/t < 2$ , and a band insulator with a completely occupied bonding band for  $t_{\perp}/t > 2$ .

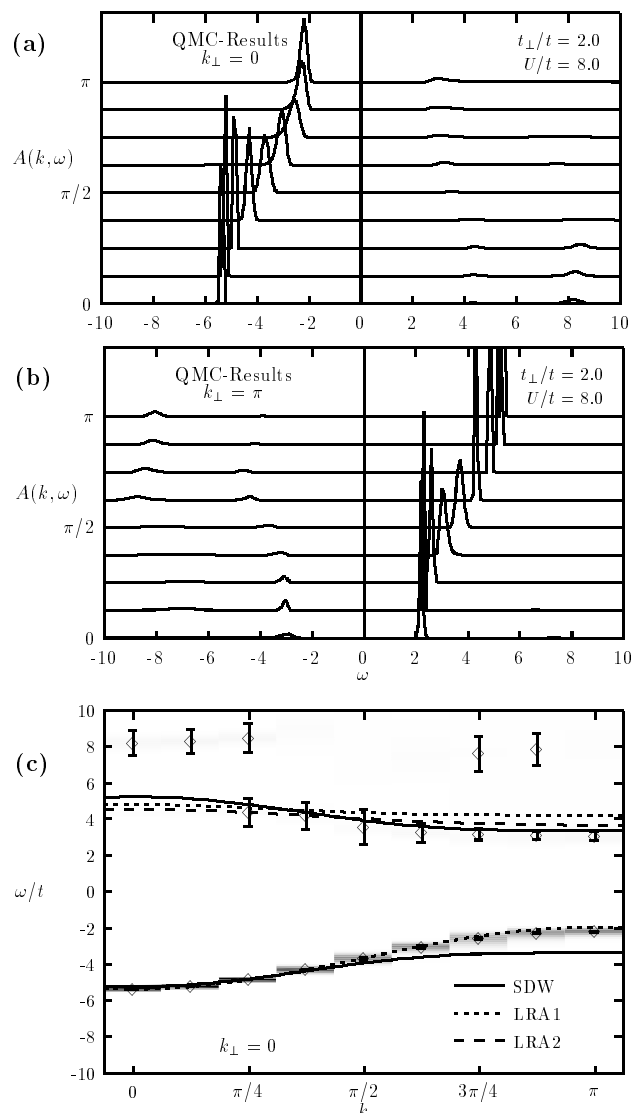


FIG. 1. QMC result for the spectral density function  $A(\mathbf{k}, \omega)$  for all possible values of  $\mathbf{k} = (k, k_{\perp})$  on a  $2 \times 16$  system with  $U/t = 8$  and  $t_{\perp}/t = 2.0$  at an inverse temperature of  $\beta = 10/t$ . Parts (a) and (b) are three-dimensional plots on the  $\omega$ - $k$  plane for  $k_{\perp} = 0$  and  $k_{\perp} = \pi$ , respectively. Part (c) is a density plot for the  $k_{\perp} = 0$  branch with darker shading corresponding to higher spectral weight, and the points with error bars showing the position of the peaks. The thick solid line indicates the SDW result within AFHF at  $T = 0$ , the dashed line is the calculated local rung approximation (LRA) dispersion for local excitations on one rung (LRA1) and the long-dashed line shows the spectrum obtained by local excitations on a four-site cluster (LRA2).

## II. SINGLE-PARTICLE SPECTRAL WEIGHT

### A. Quantum Monte Carlo Results

In order to calculate the dynamical properties of the above model we employ the grand-canonical Quantum

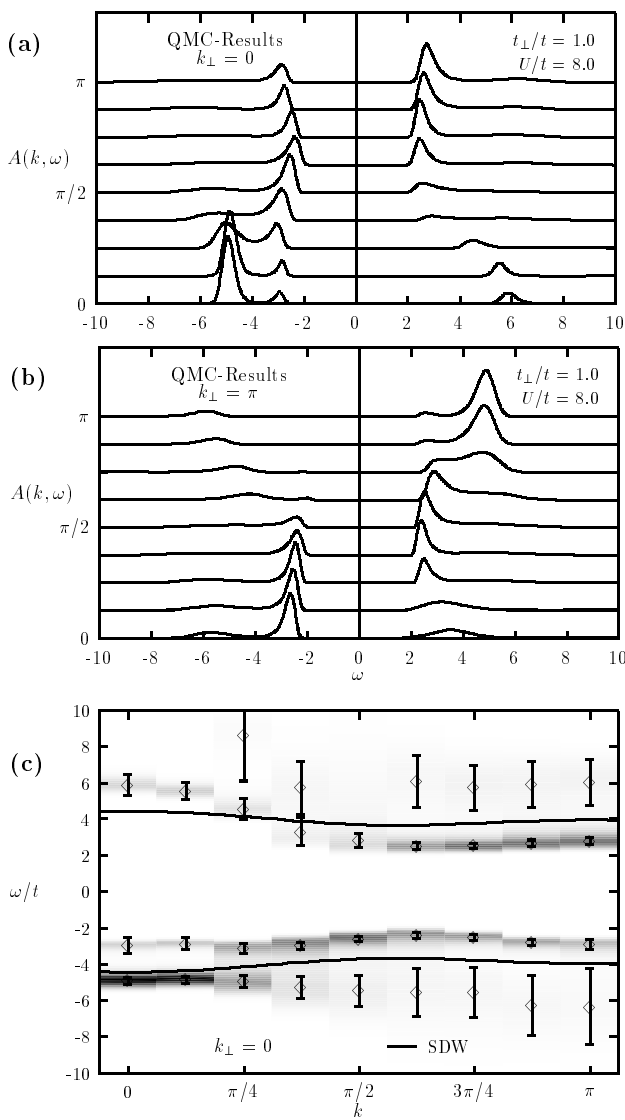


FIG. 2. The single particle spectral weight  $A(\mathbf{k}, \omega)$  as in Fig. 1, with the same parameters except with an isotropic hopping,  $t_{\perp}/t = 1.0$ . In (c), the solid line is the SDW result calculated within AFHF.

Monte Carlo (QMC) algorithm to determine the expectation values of the correlation functions in imaginary time. At half-filling, the simulations are not limited by the fermion sign problem and accurate results can thus be achieved at low temperatures and large system sizes. We analytically continue the imaginary-time data to real frequencies using a Maximum Entropy method<sup>10</sup>. For example, the spectral weight function given by

$$A(\mathbf{k}, \omega) = \frac{1}{Z} \sum_{l, l'} e^{-\beta E_l} (1 + e^{-\beta \omega}) | \langle l | c_{\mathbf{k}, \uparrow} | l' \rangle |^2 \cdot \delta(\omega - (E_{l'} - E_l)), \quad (3)$$

where  $Z$  is the partition function,  $|l\rangle$  and  $|l'\rangle$  are the exact many-body eigenstates with the corresponding

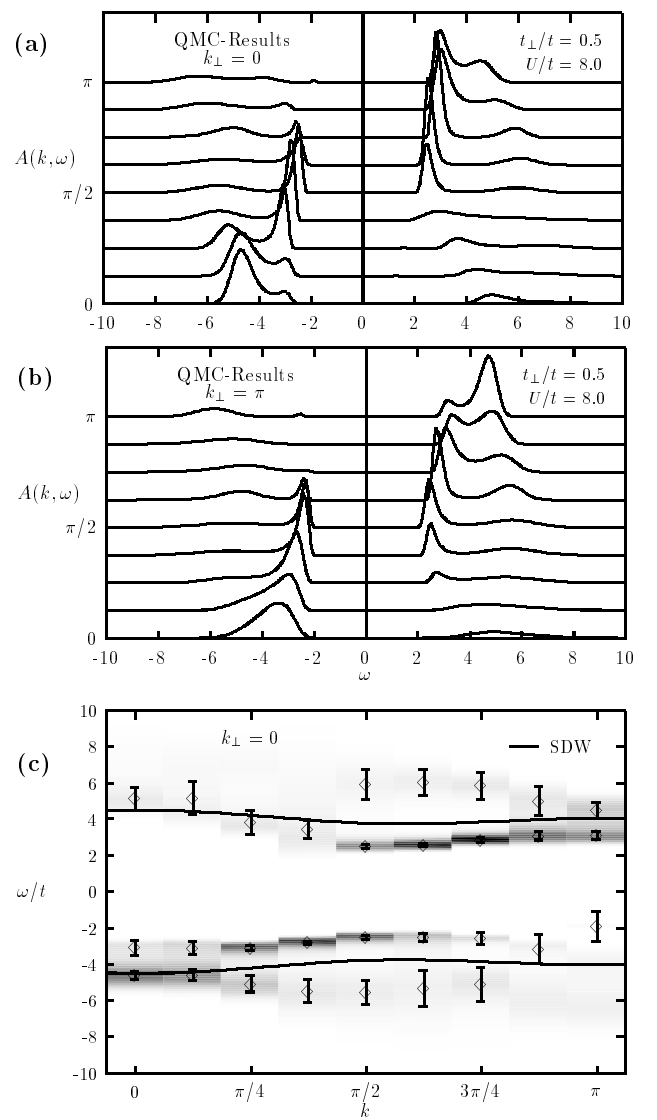


FIG. 3. The single particle spectral weight  $A(\mathbf{k}, \omega)$  as in Fig. 1, with the same parameters except with  $t_{\perp}/t = 0.5$ . In (c), the solid line is the SDW result calculated within AFHF.

energies  $E_l$  and  $E_{l'}$  and  $c_{\mathbf{k}, \sigma} = \sum_{i, \lambda} c_{i, \lambda \sigma} e^{i\mathbf{k} \cdot \mathbf{R}_{i, \lambda}} / \sqrt{2L}$ , can be calculated by inverting the spectral theorem

$$G(\mathbf{k}, \tau) \equiv \langle c_{\mathbf{k}, \uparrow}(\tau) c_{\mathbf{k}, \uparrow}^\dagger(0) \rangle = \int_{-\infty}^{\infty} \frac{e^{-\tau \omega}}{1 + e^{-\beta \omega}} A(\mathbf{k}, \omega) d\omega \quad (4)$$

with the Maximum Entropy algorithm using the raw QMC data  $G(\mathbf{k}, \tau)$ . To achieve high resolution, it is important to use a likelihood function which takes the error-covariance matrix of the QMC data and its statistical inaccuracy consistently into account<sup>16</sup>. The results presented here are based on QMC data with good statistics, i.e. averages over  $10^5$  updates of all the Hubbard-Stratonovich variables result in  $G(\mathbf{k}, \tau)$ 's with absolute errors less than or of the order of  $5 \times 10^{-4}$ . Correlations of the data in imaginary time were taken into account

by making use of the covariance matrix in the Maximum Entropy procedure<sup>16</sup>. As suggested in previous work by White<sup>17</sup>, various moments of the spectral weight were also incorporated in extracting  $A(\mathbf{k}, \omega)$ .

We calculate the spectral function  $A(\mathbf{k}, \omega)$  at half-filling for a  $2 \times 16$ -lattice with  $U/t = 8$  for different values of  $t_{\perp}$  at an inverse temperature of  $\beta = 10/t$ . Our results are given in Fig. 1 for  $t_{\perp}/t = 2.0$ , in Fig. 2 for  $t_{\perp}/t = 1.0$ , and in Fig. 3 for  $t_{\perp}/t = 0.5$ . Note that  $t_{\perp}/t = 1.0$  corresponds to the isotropic case,  $J_{\perp} \approx J$ , relevant to the  $\text{SrCu}_2\text{O}_3$ ,  $(\text{VO})_2\text{P}_2\text{O}_7$ , and  $\text{LaCuO}_{2.5}$  compounds. Parts (a) and (b) in Fig. 1–3 are three-dimensional plots of  $A(\mathbf{k}, \omega)$  versus  $\omega$  for  $k$ -values in the 1D Brillouin zone, whereas part (c) in all three figures summarize these results in the usual “band structure”  $\omega$  versus  $k$  plot. The shaded areas represent regions with significant spectral weight, with the darker shading representing more weight. Due to particle-hole symmetry,  $A(\mathbf{k} = (k, \pi), \omega) = A(\mathbf{k} = (\pi - k, 0), -\omega)$  where  $\mathbf{k} = (k, k_{\perp})$ . In other words, one reflects  $k$  about  $k = \pi/2$  and  $\omega$  about 0 to get  $A(\mathbf{k}, \omega)$  for  $k_{\perp} = \pi$  from  $A(\mathbf{k}, \omega)$  for  $k_{\perp} = 0$ . This symmetry can be seen by comparing parts (a) and (b) of Fig. 1–3. Since this symmetry is not enforced by the Maximum Entropy procedure, it is only present approximately, and the extent to which the reflected spectra at  $k_{\perp} = 0$  do not match those at  $k_{\perp} = \pi$  gives an indication of the accuracy of the analytic continuation procedure. In the density plots in parts (c), we show only the  $k_{\perp} = 0$  components. For  $t_{\perp}/t = 2.0$ , there is a heavily weighted coherent band of width  $\sim 3t$  in the photoemission ( $\omega < 0$ ) part of the spectrum. In the inverse photoemission spectrum ( $\omega > 0$ ) there is very little total spectral weight. There are therefore two bands with significant spectral weight, one in the photoemission spectrum for  $k_{\perp} = 0$  and one in the inverse photoemission spectrum for  $k_{\perp} = \pi$ . Each band is about  $2t$  away from the Fermi surface, leading to a gap of approximately  $4t$ . Therefore, for large  $t_{\perp}$ , the system is a two-band insulator.

In contrast, for  $t_{\perp}/t = 1.0$  and  $t_{\perp}/t = 0.5$ ,  $A(\mathbf{k}, \omega)$  has substantial spectral weight in four bands, one in the photoemission spectrum ( $\omega < 0$ ) for  $k_{\perp} = 0$  and  $k_{\perp} = \pi$  and one in the inverse photoemission spectrum ( $\omega > 0$ ) for both values of  $k_{\perp}$ . In this regime, the system is thus a four-band insulator. For  $t_{\perp}/t = 0.5$  (Fig. 3) the spectral weight is present for both values of  $k_{\perp}$  concentrated between  $k = 0$  and  $k = \pi/2$  in the photoemission part and between  $k = \pi/2$  and  $k = \pi$  in the inverse photoemission part of the spectrum. For the isotropic case ( $t_{\perp}/t = 1.0$ , Fig. 2), there is some shift of spectral weight to the photoemission part for  $k_{\perp} = 0$  and to the inverse photoemission part for  $k_{\perp} = \pi$ . The maxima of the photoemission band in the  $k_{\perp} = 0$  part occurs at  $k^* = \pi$  for  $t_{\perp}/t = 2.0$ , at  $k^* \approx 0.7\pi$  for  $t_{\perp}/t = 1.0$ , and at  $k^* = \pi/2$  for  $t_{\perp}/t = 0.5$ . Therefore we would expect to see a maxima at  $k^* \approx 0.7\pi$  in a photoemission experiment on the isotropic ladder compounds, an experiment which has, to our knowledge, not yet been done.

It is also important to note that the QMC  $A(\mathbf{k}, \omega)$  results for  $t_{\perp}/t = 0.5$  as well as for the isotropic case,  $t_{\perp}/t = 1.0$ , display two general features which have recently been observed in both the 1D<sup>13</sup> and 2D<sup>14</sup> cases using the improved Maximum Entropy techniques described above<sup>16</sup>. One feature is that  $A(\mathbf{k}, \omega)$  contains a rather dispersionless “incoherent background” extending over several  $t$  ( $\sim 6t$  for  $U/t = 8$  in 2D) in both the electronically occupied ( $\omega < 0$ ) and unoccupied ( $\omega > 0$ ) parts of the spectrum. The crucial structure, not resolved in previous 1D and 2D QMC simulations, is a dispersive structure at low energies with a small width of the order of the exchange coupling  $J = 4t^2/U$ . It is this latter coherent “band” which defines the gap  $\Delta$  and which, for larger  $U$  ( $U/t \sim 10$ ), is well-separated from the higher-energy background. As in the 1D and 2D cases, the splitting in the low-energy band and the higher-energy background is especially pronounced near  $k = 0$  and  $k = \pi$  due to a relative weight shift from negative to positive energies as  $k$  moves through  $k^*$ .

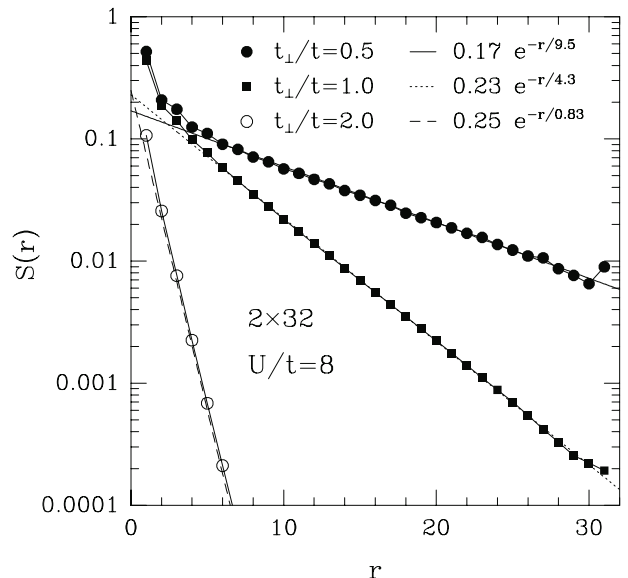


FIG. 4. The spin-spin correlation function  $S(r)$  for  $t_{\perp} = 2t$ ,  $t_{\perp} = t$  and  $t_{\perp} = 0.5t$  calculated on a  $2 \times 32$  lattice with  $U/t = 8$  and open boundary conditions using the DMRG. The solid, dotted and dashed lines are asymptotic fits to the data using the simple exponential form  $A \exp(-r/\xi)$ .

## B. Spin-Wave Theory

At half-filling, the two chain Hubbard system at  $T = 0$  is a spin liquid with a spin gap and a finite spin-spin correlation length. The system is therefore less ordered than either the 1D system, which is at the critical point and has power law decay of the spin-spin correlation function and no spin gap, or the 2D system, which has long-range spin order and gapless spin-wave-like excitations. However, at large  $U/t$  the scale of the spin gap for the two chain system is set by  $J_{\perp} \sim 4t_{\perp}^2/U$ ,

and the spin-spin correlation length  $\xi$  grows longer as the spin gap gets smaller. The range of the spin ordering can therefore be tuned by varying  $t_{\perp}/t$ . This is illustrated by Fig. 4, in which we plot the spin-spin correlation function,  $S(r) = (-1)^r \langle M_{0,\lambda}^z M_{r,\lambda}^z \rangle$  on a semilog scale for  $t_{\perp}/t = 2.0$ ,  $t_{\perp}/t = 1.0$  and  $t_{\perp}/t = 0.5$ . Here  $M_{r,\lambda}^z = (n_{r,\lambda,\uparrow} - n_{r,\lambda,\downarrow})$  is twice the  $z$  component of the on-site spin. These calculations were done using the Density Matrix Renormalization Group method<sup>8</sup> (DMRG) on a system with open boundaries at zero temperature. For  $t_{\perp}/t = 0.5$ , the data was averaged over a number of different pairs of points for a given  $r$  in order to reduce oscillations due to the open boundaries. For distances greater than a few lattice spacings, the correlation functions are very well fit by a pure exponential form  $A \exp(-r/\xi)$ , from which the spin-spin correlation length  $\xi$  can be determined. For  $t_{\perp}/t = 2.0$ ,  $\xi = 0.83$ , for  $t_{\perp}/t = 1.0$ ,  $\xi = 4.3$ , and for  $t_{\perp}/t = 0.5$ ,  $\xi = 9.5$  lattice spacings. Therefore, the spins are almost completely uncorrelated along the chains for  $t_{\perp}/t = 2.0$ , but for  $t_{\perp}/t = 1.0$  and for  $t_{\perp}/t = 0.5$  are correlated on length scales of the order of the size of the  $2 \times 16$  lattice studied here, although the long-range behavior is that of a gapped spin liquid in all three cases.

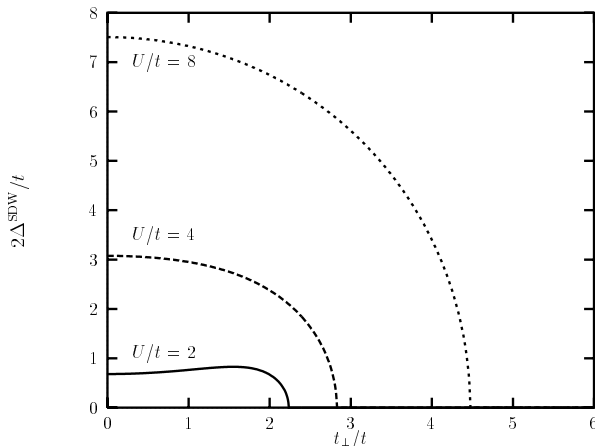


FIG. 5. The SDW gap calculated within the AFHF approximation at  $T = 0$ , as a function of  $t_{\perp}/t$  on a  $2 \times 100$  grid for  $U/t = 2, 4, 8$ .

It is therefore reasonable to calculate the single particle spectral weight  $A(\mathbf{k}, \omega)$  in two simple ways: first, when the spin gap is small and  $\xi \approx L$ , and we consider wavelengths smaller than  $\xi$  and frequencies larger than the spin gap, it is useful to explore the consequences of a simple SDW approximation based on an ordered state, i.e. AFHF theory. Secondly, one can solve for the exact eigenstates on a rung and then consider states composed of a product of exact rung singlets only and a delocalized one-hole state in a background of rung singlets. (We call this the Local Rung Approximation, LRA.) The LRA starts with a state with uncorrelated rungs and then treats the interactions between rungs perturbatively, and is thus a good starting point when  $\xi$  is small. As we shall

see, the LRA gives a single particle spectral weight distribution that agrees well with QMC in the large  $t_{\perp}$  regime, while AFHF qualitatively describes most features of the spectral weight distribution for small  $t_{\perp}$ .

We first discuss the AFHF calculation in more detail. The Hartree-Fock one-particle Hamiltonian can be written as

$$H_{HF} = \sum'_{\mathbf{k}, \sigma} E_{\mathbf{k}} (b_{\mathbf{k}, \sigma}^{\dagger} b_{\mathbf{k}, \sigma}^c - b_{\mathbf{k}, \sigma}^{v\dagger} b_{\mathbf{k}, \sigma}^v), \quad (5)$$

where  $\sum'_{\mathbf{k}, \sigma}$  means that the sum runs only over the magnetic zone ( $-\pi/2 < k \leq \pi/2$ ,  $k_{\perp} = 0, \pi$ ). The operators  $b_{\mathbf{k}, \sigma}^c$  and  $b_{\mathbf{k}, \sigma}^v$  are given by the following transformation<sup>18</sup>:

$$b_{\mathbf{k}, \sigma}^c = u_{\mathbf{k}} c_{\mathbf{k}, \sigma} \mp v_{\mathbf{k}} c_{\mathbf{k}+\mathbf{Q}, \sigma}, \quad (6)$$

$$b_{\mathbf{k}, \sigma}^v = v_{\mathbf{k}} c_{\mathbf{k}, \sigma} \pm u_{\mathbf{k}} c_{\mathbf{k}+\mathbf{Q}, \sigma}, \quad (7)$$

where  $\mathbf{Q} = (\pi, \pi)$ , the upper (lower) sign corresponds to  $\sigma = \uparrow$  ( $\sigma = \downarrow$ ), and

$$u_{\mathbf{k}} = \sqrt{\frac{1}{2}(1 + \varepsilon_{\mathbf{k}}/E_{\mathbf{k}})}, \quad (8)$$

$$v_{\mathbf{k}} = \sqrt{\frac{1}{2}(1 - \varepsilon_{\mathbf{k}}/E_{\mathbf{k}})}, \quad (9)$$

$$E_{\mathbf{k}} = \sqrt{\Delta^2 + \varepsilon_{\mathbf{k}}^2}. \quad (10)$$

Here  $\varepsilon_{\mathbf{k}}$  is the free particle energy ( $U = 0$ ) defined in Eq. (2). The spin-density-wave gap,  $\Delta$ , is self-consistently determined by the equation

$$\frac{1}{U} = \frac{1}{2L} \sum'_{\mathbf{k}} \frac{1}{E_{\mathbf{k}}}. \quad (11)$$

The band structure of the AFHF Hamiltonian is given by  $\pm E_{\mathbf{k}} = \pm \sqrt{\Delta^2 + \varepsilon_{\mathbf{k}}^2}$  in the magnetic Brillouin zone. The SDW gap  $\Delta$ , calculated by solving Eq. (11) self-consistently, is shown as a function of  $t_{\perp}/t$  for  $U/t = 2, 4$ , and  $8$  in Fig. 5. The transition from a two-band metal to a band insulator in the  $U = 0$  system occurs at  $t_{\perp}/t = t_{\perp c} = 2.0$ . As  $U$  is turned on for  $t < t_{\perp c}$  in the AFHF, a gap develops in both the bonding and antibonding bands, leading to a four-band insulator. If  $t_{\perp}$  is then increased,  $\Delta$  will go to zero at approximately the noninteracting ( $U = 0$ )  $t_{\perp c}/t = 2.0$ , as seen for  $U/t = 2$  in Fig. 5, leading to a transition from a four-band to a two-band insulator. For large  $U$  and small  $t_{\perp}$ ,  $\Delta \approx U/2$ , as seen for  $U/t = 8$  in Fig. 5, so the Coulomb splitting of the bands will dominate over  $U = 0$  band structure effects. In this case, the gap will go to zero, i.e. the system will undergo a transition to a band insulator only when the band structure splitting  $2t_{\perp}$ , is of the order of the Coulomb splitting, so that  $t_{\perp c} \approx \Delta \approx U/2$ .

The spectral weight within the AFHF approximation is

$$A(\mathbf{k}, \omega) = u_{\mathbf{k}}^2 \delta(\omega - E_{\mathbf{k}}) + v_{\mathbf{k}}^2 \delta(\omega + E_{\mathbf{k}}). \quad (12)$$

We show the spectral weight  $A(\mathbf{k}, \omega)$  from AFHF for the same parameters as in Fig. 1 and Fig. 3 in Fig. 6(a) for  $t_{\perp}/t = 2.0$  and Fig. 6(b) for  $t_{\perp}/t = 0.5$ . The band splitting  $2\Delta \approx U$  in both cases, as can also be seen in Fig. 5. Since both the bonding and antibonding bands are split by this gap, there are two peaks in  $A(\mathbf{k}, \omega)$  as a function of  $\omega$  for each  $\mathbf{k}$ , leading to a four-band insulator for both values of  $t_{\perp}/t$ . Since the band splitting is set by  $U$  rather than  $2t_{\perp}$ , the spectral weight is almost evenly distributed between two coherent bands for both  $t_{\perp}/t = 2.0$  and  $t_{\perp}/t = 0.5$ . Therefore, for  $t_{\perp}/t = 2.0$ , as can be seen by comparing the QMC results in Fig. 1 with Fig. 6(a), the AFHF spectral weight distribution for  $t_{\perp}/t = 2.0$  is completely wrong, with too much weight in the upper,  $\omega > 0$ , band for  $k_{\perp} = 0$  and the  $\omega < 0$  band for  $k_{\perp} = \pi$ . While the average positions of the AFHF bands, shown as thick solid lines in Fig. 1(c), are approximately the same as those of the QMC bands, the band widths are too small by approximately a factor of two. For  $t_{\perp}/t = 2.0$  and  $U/t = 8$ , then, the AFHF calculation results in a four-band insulator in which there is long-range antiferromagnetic order, while the QMC results show that the system is a two-band insulator, with only very short range antiferromagnetic correlations. While the AFHF picture does produce a two-band insulator for  $t_{\perp}/t \gtrsim 4.5$ , the physical picture of the transition to this phase is quite different (see section C).

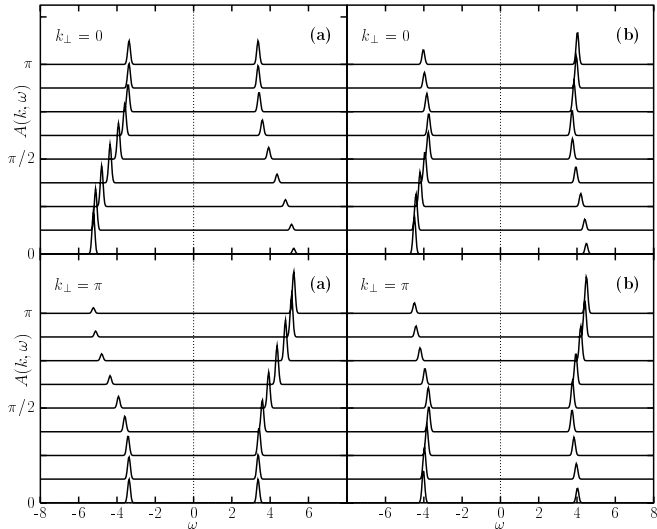


FIG. 6. Spectral weight calculated within the AFHF approximation for (a)  $t_{\perp}/t = 2.0$  and (b)  $t_{\perp}/t = 0.5$  with  $U/t = 8$ , shown for  $k_{\perp} = 0$  and  $k_{\perp} = \pi$ .

For  $t_{\perp}/t = 0.5$ , as seen in Fig. 3 and Fig. 6(b), AFHF gives two dispersive bands in the  $k_{\perp} = 0$  branch of width of order  $J \sim 4t^2/U$ , similar to the coherent bands seen in the QMC data. However, in the AFHF, the single particle gap is somewhat too large, the weight distribution extends too far towards  $k = \pi$  and too far towards  $k = 0$  for the photoemission and inverse photoemission parts of the spectrum, respectively, and the broad inco-

herent background is not present. We have also carried out mean-field slave boson calculations<sup>20</sup> in order to try to improve on the AFHF picture. These calculations give a gap about 15% smaller than AFHF, and a bandwidth about 3% smaller, but do not qualitatively improve on the AFHF calculations. The same holds for  $t_{\perp}/t = 1.0$ , where the AFHF describes approximately the coherent part of the spectrum and also produces a too large single particle gap and a slightly different spectral weight distribution. Therefore, for  $t_{\perp}/t = 0.5$  and for  $t_{\perp}/t = 1.0$ , AFHF would give a reasonable description of the dispersion and general spectral weight distribution of the coherent spin-wave bands, if the gap were phenomenologically adjusted to a smaller value, but fails to even qualitatively describe the spectral weight distribution for  $t_{\perp}/t = 2.0$ .

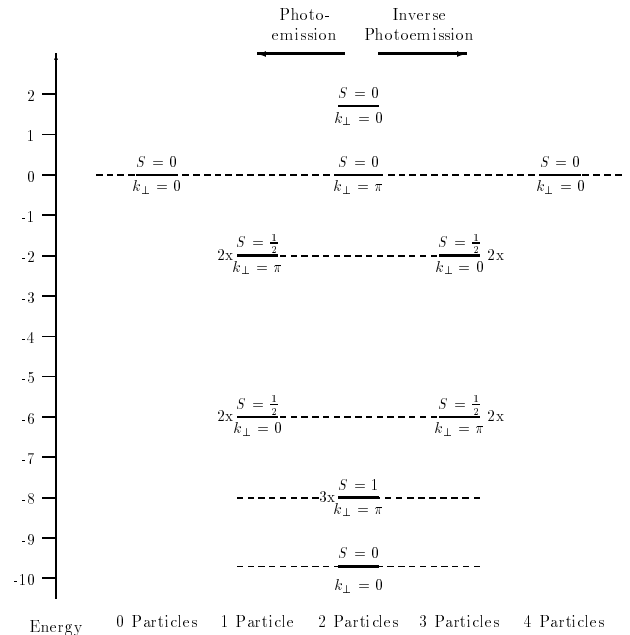


FIG. 7. Exact eigenstates for a two-site system representing a disconnected rung, with  $U = 8$  and  $t_{\perp} = 2.0$ . The horizontal axis is the number of particles and the vertical axis shows the total energy  $\langle (H - \mu N) \rangle$ , where the chemical potential  $\mu = U/2$  at half-filling. Each level is labeled with the total spin  $S$  and momentum  $k_{\perp}$ .

### C. Local Rung Approximation

For very large  $t_{\perp}$ , a better starting point is the limit of weak interaction between the rungs. In this limit, we split the Hamiltonian of Eq. (1) into  $H = H_0 + H_I$  with

$$H_0 = -t_{\perp} \sum_{i,\sigma} (c_{i,1\sigma}^{\dagger} c_{i,2\sigma} + h.c.) + U \sum_{i\lambda} n_{i,\lambda} \uparrow n_{i,\lambda} \downarrow,$$

$$H_I = -t \sum_{i,\lambda\sigma} (c_{i,\lambda\sigma}^{\dagger} c_{i+1,\lambda\sigma} + h.c.), \quad (13)$$

where  $H_0$  denotes the non-interacting rung limit. The ground state of  $H_0$  is a product of individual rung ei-

genstates. Accordingly, we first diagonalize the Hubbard Hamiltonian on the two sites making up the rung in order to find the rung eigenstates. A schematic diagram of the exact eigenstates for a single rung is shown in Fig. 7. The ground state for the half-filled rung  $i$  (two particles per rung) is a spin singlet state with  $k_{\perp} = 0$  and energy  $E_0/L = E_0^{\text{rung}} = (U - \sqrt{U^2 + 16t_{\perp}^2})/2$  denoted by  $|S_i\rangle$ . For large values of  $U$ , the energy of this two-site state is given by the exchange coupling  $-J_{\perp} \sim -4t_{\perp}^2/U$ . Note that  $|S_i\rangle$  contains terms which have double occupied sites as well as the usual singlet construction  $(|\uparrow, \downarrow\rangle - |\downarrow, \uparrow\rangle)/\sqrt{2}$ .

We can then form an approximation to the ground state for the half-filled system by taking a state which is just a product of the rung states,

$$|\psi_0\rangle = |S_1\rangle|S_2\rangle\dots|S_L\rangle. \quad (14)$$

For  $t_{\perp}/t = 2.0$ , the binding energy of a singlet formed on a rung is about four times lower than the energy of a singlet between neighboring sites along a chain, and therefore we expect  $|\psi_0\rangle$  to be a good approximation to the exact ground state.

In order to obtain the  $\omega < 0$  spectral weight for the half-filled system, we need to calculate the matrix element of  $c_{\mathbf{k},\sigma}$  given in Eq. (3). In other words, we need matrix elements between a half-filled state and a state with one particle removed. We form the approximate one hole state by replacing one bond singlet state at rung  $\ell$ ,  $|S_{\ell}\rangle$ , with the lowest energy one-particle state, the one with bonding ( $k_{\perp} = 0$ ) symmetry,  $|B_{\ell 1}\rangle$  (We remove a spin down electron for definiteness.) and define

$$|\ell\rangle = |S_1\rangle|S_2\rangle\dots|B_{\ell 1}\rangle\dots|S_L\rangle. \quad (15)$$

We delocalize the single-particle state with a plane wave ansatz by constructing the state<sup>6,21</sup>

$$|\psi_1(k)\rangle = L^{-1/2} \sum_{\ell=1}^L e^{ik\ell} |\ell\rangle. \quad (16)$$

Trivially, this state is an exact eigenstate of  $H_0$ . We will take this state as the ground state for the system with one hole with momentum  $\mathbf{k} = (k, 0)$ . The spectral weight  $A(\mathbf{k}, \omega)$  at zero temperature ( $\beta \rightarrow \infty$ ) is then approximated by using only the two states  $|\psi_0\rangle$  and  $|\psi_1(k)\rangle$  in Eq. (3). For  $k_{\perp} = 0$ , the energy dispersion  $\omega(k)$  of  $A(\mathbf{k}, \omega)$  for  $\omega < 0$  is given by

$$\begin{aligned} \omega(k) &= \langle \psi_0 | H | \psi_0 \rangle - \langle \psi_1(k) | H | \psi_1(k) \rangle - \mu \\ &= -\frac{1}{2} \sqrt{U^2 + 16t_{\perp}^2} + t_{\perp} - tA \cos k, \end{aligned} \quad (17)$$

with  $A = (1 + E_2/2t_{\perp})^2 / (1 + E_2^2/4t_{\perp}^2)$ ,  $E_2 = (U + \sqrt{U^2 + 16t_{\perp}^2})/2$ , and the corresponding spectral weight by  $|\langle \psi_1(k) | c_{k,1} | \psi_0 \rangle|^2$ . The dispersion given by Eq. (17) for  $U/t = 8$  and  $t_{\perp}/t = 2.0$  is plotted in Fig. 1(c) and the spectral weight for  $k_{\perp} = 0$  is shown in Fig. 8. One

can see that the position of the peak of the  $\omega < 0$  LRA band, denoted LRA1 in Fig. 1(c), lays almost exactly on the QMC data. However, the position and the dispersion of the  $\omega > 0$  band, which were obtained in the same way as for  $\omega < 0$ , are not exactly matched by the LRA1 calculation. While this band is not very important in the sense that it contains very little spectral weight, we can understand how to improve the LRA1 calculation by considering the states of a four site cluster.

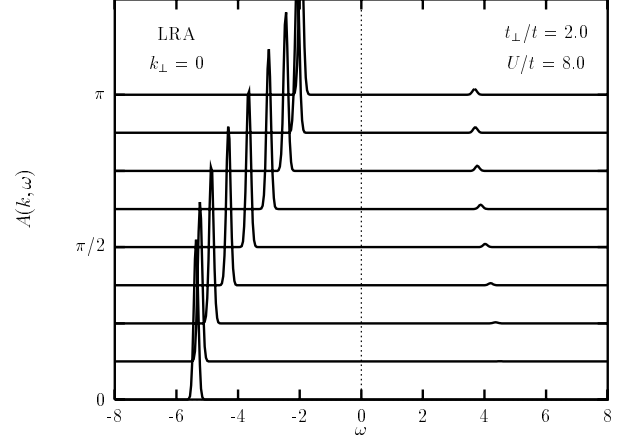


FIG. 8. Spectral weight using LRA1 calculation for the  $\omega < 0$  and the LRA2 calculation for the  $\omega > 0$  parts of the spectrum for  $k_{\perp} = 0$ . Here  $t_{\perp}/t = 2.0$  and  $U/t = 8$ .

In order to generate the inverse photoemission spectrum, we need to calculate matrix elements between the half-filled state and a state with one *additional* particle. From Fig. 7, we see that a rung state with three particles and  $k_{\perp} = 0$  has approximately twice the excitation energy of the  $k_{\perp} = 0$  one-particle state which is relevant for the photoemission part of the spectrum. (Recall that due to the particle-hole symmetry at half-filling, this state will map to one in the inverse photoemission part of spectrum for  $k = \pi$ ; one can see this symmetry in Fig. 7.) Since the relevant three-particle single rung state is high in energy, configurations involving intrachain effects might also be important. We include the effect of such configurations by replacing two rung singlet states by the lowest energy state of five particles on four sites in the bonding channel. We can then form a delocalized plane wave state from this state as in Eq. (16). The results of this calculation are labeled as LRA2 in Fig. 1(c). The location and width of the  $k_{\perp} = 0$  inverse photoemission band are more closely fit than by the LRA1 calculation. In Fig. 8 the spectral weight distribution of the LRA1 calculation for the photoemission part of the spectrum ( $\omega < 0$ ) and the distribution of the LRA2 calculation for the inverse photoemission part ( $\omega > 0$ ) is plotted. The result is in good accordance with the QMC data in Fig. 1(a).



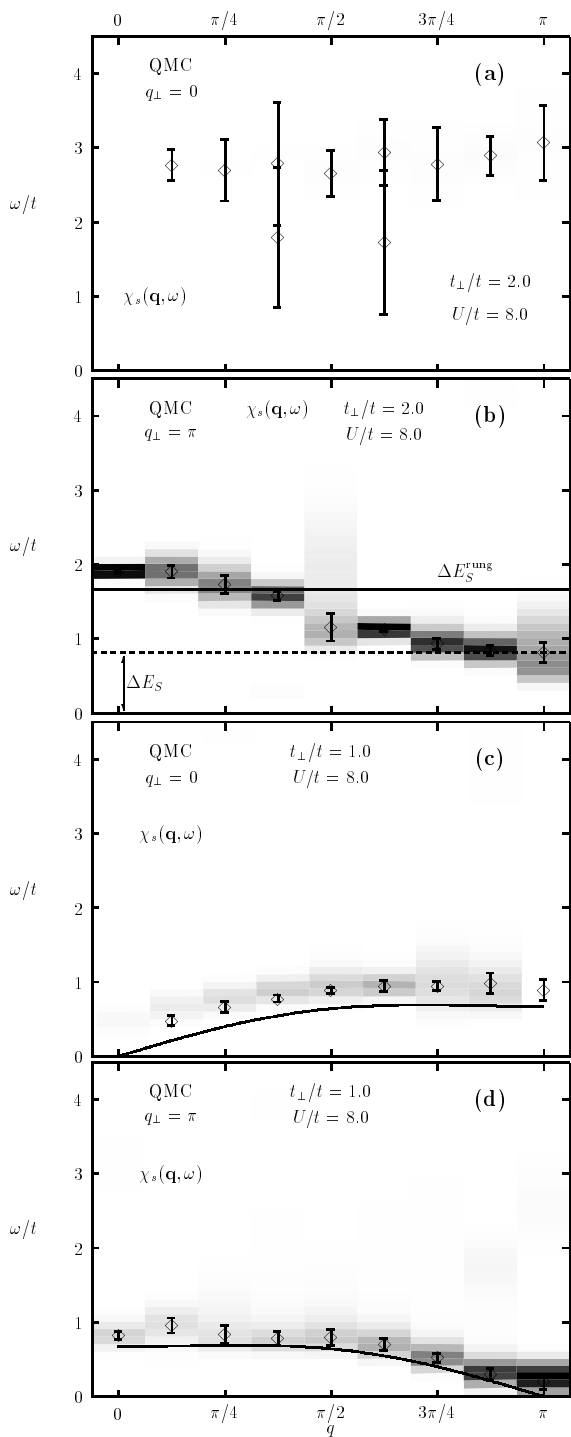


FIG. 9. Dynamic spin response function  $\chi_s(\mathbf{q}, \omega)$  for (a)  $t_{\perp}/t = 2.0$ ,  $q_{\perp} = 0$ , (b)  $t_{\perp}/t = 2.0$ ,  $q_{\perp} = \pi$ , (c)  $t_{\perp}/t = 1.0$ ,  $q_{\perp} = 0$ , and (d)  $t_{\perp}/t = 1.0$ ,  $q_{\perp} = \pi$ . Again,  $U/t = 8$  on a  $2 \times 16$  lattice. The weight of sizable structures is represented by the strength of shading in the shaded regions and the position of the maxima by the points with error bars. In (b), the solid line indicates the spin gap  $\Delta E_S^{\text{rung}}$  of the two-site system and the dashed line the spin gap  $\Delta E_S$  for the  $2 \times 16$  ladder at  $T = 0$ , calculated with a projector QMC algorithm. In (c) and (d), the solid lines are  $\chi_{\text{RFA}}^{\pm}(\mathbf{q}, \mathbf{q}, \omega)$  calculated using the SDW approximation given by Eq. (19).

In order to determine the nature of the low lying excitations, we also consider the spin and charge susceptibilities  $\chi_{s,c}(\mathbf{q}, \omega)$  which, in a Lehmann representation, are defined as

$$\chi_{s,c}(\mathbf{q}, \omega) = \frac{i}{Z} \sum_{l,l'} e^{-\beta E_l} (1 - e^{-\beta \omega}) |\langle l | O_{s,c}(\mathbf{q}) | l' \rangle|^2 \cdot \delta(\omega - (E_{l'} - E_l)), \quad (18)$$

with  $O_s(\mathbf{q}) = \sum_{\mathbf{p}} (c_{\mathbf{p}+\mathbf{q},\uparrow}^{\dagger} c_{\mathbf{p},\uparrow} - c_{\mathbf{p}+\mathbf{q},\downarrow}^{\dagger} c_{\mathbf{p},\downarrow})$  and  $O_c(\mathbf{q}) = \sum_{\mathbf{p},\sigma} c_{\mathbf{p}+\mathbf{q},\sigma}^{\dagger} c_{\mathbf{p},\sigma}$ . We calculate the two-particle dynamic response from the two-particle imaginary time Green's function, as in Eq. (4) and use the Maximum Entropy method described above for the analytical continuation of  $\chi_{s,c}(\mathbf{q}, \omega)$  to real frequencies.

In Fig. 9 we show the dynamical spin-spin correlation function  $\chi_{s,c}(\mathbf{q}, \omega)$  for  $t_{\perp}/t = 2.0$  and  $t_{\perp}/t = 1.0$ . For  $t_{\perp}/t = 2.0$ , the  $q_{\perp} = 0$  component [Fig. 9(a)] has a broad, lightly weighted structure centered approximately at  $\omega = 3t$ , with the spectral weight vanishing for small  $q$ . For  $q_{\perp} = \pi$  [Fig. 9(b)], there is a coherent, dispersive band with a width set by  $J \approx 4t^2/U = 0.5t$ , a minimum at  $q = \pi$  and a maximum at  $q = 0$ . The minimum spin gap is approximately  $0.8t$ , which agrees well with the value we obtain using Projector Quantum Monte Carlo, indicated by the dashed line on the plot. The spectral weight is most heavily concentrated around  $q = \pi$ .

The dynamic spin response at half-filling measures the response of the system to spin triplet excitations. Since here  $t_{\perp}$  is large, we consider the effect of triplet excitations on product rung states of the type considered in Eq. (14), in the LRA calculation. A triplet excitation will change the total spin of the state from  $S = 0$  to  $S = 1$ . Referring to Fig. 7, the only triplet excited state on a single rung has momentum  $\pi$  (corresponding to odd parity under chain interchange) leading to a change in momentum  $q_{\perp} = \pi$  for the triplet excitation. The size of this triplet excitation  $\Delta E_S^{\text{rung}}$  is marked on Fig. 9(b) by the solid line. This local triplet excited state can be moved to a near neighbor rung by a process which is second order in  $H_I$ . The local triplet excited states can then be delocalized into a Bloch wave as in Eq. (15) and Eq. (16). For large  $U$ , one then obtains a dispersion relation of the form  $\Delta E_S^{\text{rung}} + J \cos q$ , where  $J \sim 4t^2/U$ , a form similar to that obtained in Ref. 5 for the two chain Heisenberg model. The coherent band in Fig. 9(b) does have a minimum at  $q = \pi$ , and has approximately this form.

Within the LRA picture, it is also possible to excite a  $q_{\perp} = 0$  (even under chain interchange) triplet excitation via a “two-magnon” process, as discussed in Ref. 5. This corresponds to making two local triplet excitations on rungs in the non-interacting rung picture, and

would lead to an excitation energy whose scale, in the Heisenberg limit, is set by  $\omega \sim 2J_{\perp}$  rather than  $\omega \sim J_{\perp}$ . The overall position of the lightly weighted band seen for  $q_{\perp} = 0$  in Fig. 9(a) is consistent with this two-magnon band, although the band is too lightly weighted and our resolution too low to extract a dispersion relation.

For the physical relevant isotropic case ( $t_{\perp}/t = 1.0$ ), shown in Fig. 9(c) and (d), the spin response looks quite different. (Because the  $t_{\perp}/t = 0.5$  results are qualitatively similar to the  $t_{\perp}/t = 1.0$  results, we show only the isotropic ( $t_{\perp}/t = 1.0$ ) case here.) In Fig. 9(c) and (d), there are dispersive bands in both the  $q_{\perp} = 0$  and  $q_{\perp} = \pi$  branches, with the position of the peak going to a finite minimum at  $\mathbf{q} = (0, \pi)$  and  $\mathbf{q} = (\pi, 0)$ , and appears to vanish as  $\mathbf{q} \rightarrow (\pi, \pi)$ . However, as shown in Fig. 4, the correlation length is 4.3 lattice spacings in this regime, and there should be a spin gap. Using DMRG calculations on lattices of  $2 \times 8$  to  $2 \times 32$  sites<sup>8</sup>, we estimate the spin gap to be of order  $0.12t$ . Due to finite size effects and finite resolution in the analytic continuation, this gap is too small to resolve in Fig. 9(d). Near  $\mathbf{q} = (0, 0)$  [Fig. 9(c)], the dispersion of the peak is hard to discern because there is very little spectral weight. This lack of spectral weight at  $\mathbf{q} = (0, 0)$  is present in all the dynamic charge and spin correlations and is due to a selection rule that comes about because  $O_{s,c}(\mathbf{q} = \mathbf{0})$  in Eq. (18) commutes with the Hamiltonian, leading to a vanishing of the matrix element of  $O_{s,c}(\mathbf{q})$  as  $\mathbf{q} \rightarrow \mathbf{0}$ . Therefore, the system has relatively long-range spin order in this regime and, to within the resolution of our calculations, shows the characteristics of an ordered state with gapless excitations. Thus it is interesting to compare the QMC spectra to the results of spin-wave theory calculations.

In order to extract the low-lying spin excitations using spin-wave theory it is necessary to consider the RPA transverse spin susceptibility  $\chi_{\text{RPA}}^{+-}(\mathbf{k}, \mathbf{k}', \omega)$ . It is obtained by applying the random-phase approximation to the response function  $\chi_0^{+-}(\mathbf{k}, \mathbf{k}', \omega)$ , which is calculated directly in real time using the AFHF ground state  $|\Omega\rangle$ , calculated in section II B:

$$\chi_0^{+-}(\mathbf{q}, \mathbf{q}', t) = \frac{i}{4L} \langle \Omega | T S_{\mathbf{q}}^+(t) S_{-\mathbf{q}'}^-(0) | \Omega \rangle, \quad (19)$$

with  $S^{\pm} = S_x \pm iS_y$ . Due to the broken spin rotational symmetry of  $|\Omega\rangle$ ,  $\chi_{\text{RPA}}^{+-}(\mathbf{q}, \mathbf{q}', \omega)$  contains a gapless mode, as predicted by the Goldstone theorem. Following the procedure of Schrieffer et al.<sup>18</sup>, one obtains:

$$\chi_{\text{RPA}}^{+-}(\mathbf{q}, \mathbf{q}', \omega) = \sum_{\mathbf{p}} \chi_0^{+-}(\mathbf{q}, \mathbf{p}, \omega) [1 - U \chi_0^{+-}(\mathbf{p}, \mathbf{q}', \omega)]^{-1}, \quad (20)$$

where  $[1 - U \chi_0^{+-}(\mathbf{p}, \mathbf{q}', \omega)]^{-1}$  is a matrix inverse of a  $2 \times 2$  matrix in  $\mathbf{q}$ -space and

$$\chi_0^{+-}(\mathbf{q}, \mathbf{q}', \omega) = \delta(\mathbf{q} - \mathbf{q}') \chi_0^{+-}(\mathbf{q}, \omega) + \delta(\mathbf{q} - \mathbf{q}' + \mathbf{Q}) \chi_{\mathbf{Q}}^{+-}(\mathbf{q}, \omega), \quad (21)$$

with  $\chi_0^{+-}(\mathbf{q}, \omega)$  and  $\chi_{\mathbf{Q}}^{+-}(\mathbf{q}, \omega)$  given by the usual “bubble” diagrams and printed in detail in Ref. 16 [up to a misprint of a factor of 2 in  $\chi_{\mathbf{Q}}^{+-}(\mathbf{q}, \omega)$ ]. The dispersion of  $\chi_{\text{RPA}}^{+-}(\mathbf{q}, \mathbf{q}, \omega)$  is indicated as a solid line in Fig. 9(c) and 9(d). The RPA spin-wave dispersion goes to zero at  $\mathbf{q} = (0, 0)$  and  $\mathbf{q} = (\pi, \pi)$ , and goes to a finite minimum at  $\mathbf{q} = (0, \pi)$  and  $\mathbf{q} = (\pi, 0)$ , consistent with the QMC data. The spin-wave velocity, the width of the bands, and the gaps at  $\mathbf{q} = (0, \pi)$  and  $\mathbf{q} = (\pi, 0)$  are also in reasonable agreement with the QMC data.

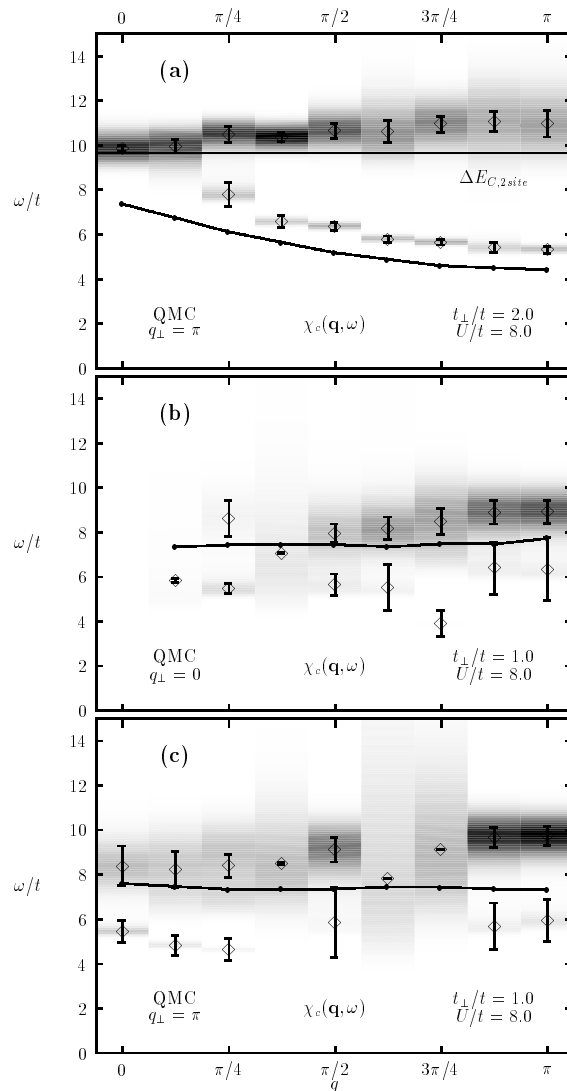


FIG. 10. The dynamic charge response function  $\chi_c(\mathbf{q}, \omega)$  for the same parameters as in Fig. 7. In (a),  $t_{\perp}/t = 2.0$  and  $q_{\perp} = \pi$ , the solid line represents the charge excitation energy on a single rung  $\Delta E_C^{\text{rung}}$ , and the line with solid dots represents the minimum excitation energy constructed from the single particle spectral weight in Fig. 1. In (b) and (c),  $t_{\perp}/t = 1.0$ , and  $q_{\perp} = 0$  and  $\pi$ , respectively. The lines with solid dots represent the minimum excitation energy of the RPA charge susceptibility  $\chi_{\text{RPA}}^{00}(\mathbf{q}, \mathbf{q}, \omega)$  calculated with the method of Ref. 16.

The QMC results for the dynamic charge correlation function are shown in Fig. 10 for  $t_{\perp}/t = 2.0$  and  $t_{\perp}/t = 1.0$ . For  $t_{\perp}/t = 2.0$ , almost all of the spectral weight is in the  $q_{\perp} = \pi$  component, so we do not show the  $q_{\perp} = 0$  component. There exist two important features: one is a heavily weighted, relatively flat band at  $\omega \sim 10t$  with heaviest weight near  $q = 0$ . This band becomes somewhat incoherent as  $q$  increases. The second is a flat, dispersive, less heavily weighted band with a minimum of order  $5t$  near  $q = \pi$ . The spectral weight in this band extends from about  $q = \pi/4$  to  $q = \pi$ , and the size of the charge gap is set by this lightly weighted lower band.

In the large  $t_{\perp}$  limit, one can understand the structure of the charge response from the LRA picture described in section II C. In the single rung picture, a charge excitation will occur through a transition to an excited state conserving the number of particles on the rung and the total spin; in other words, the important transition will be in the middle column of Fig. 7, from the low-lying  $S = 0$  state to the higher  $S = 0$  states. There are two possible charge excited states on the rung, one with momentum  $k_{\perp} = 0$  (even parity) and one with momentum  $k_{\perp} = \pi$  (odd parity). In a single rung picture, an optical transition from the  $k_{\perp} = 0$  ground state to a  $k_{\perp} = 0$  excited state is forbidden because the  $q_{\perp} = 0$  density operator  $O_c(0)$  commutes with the Hamiltonian. This selection rule forbidding a  $q_{\perp} = 0$  optical transition remains present when the rung charge excited states are constructed as in Eq. (15) and delocalized in a state like that in Eq. (16). This is why there is almost no spectral weight in the  $q_{\perp} = 0$  portion of the charge response for  $t_{\perp}/t = 2.0$ . Of course, the system is not exactly in a LRA state, so there will be some higher order processes that will introduce a very small amount of spectral weight into the  $q_{\perp} = 0$  branch. The energy of the  $q_{\perp} = \pi$  single rung transition, indicated by a solid line on the Fig. 10(a), gives an excitation energy that agrees well with energy of the heavily weighted region at  $q = 0$ .

In order to qualitatively understand the origin of the dispersion of the charge response, one can consider the possible particle-hole excitations within the one-particle band structure given by  $A(\mathbf{k}, \omega)$  in Fig. 1. There will be significant amplitude in the two-particle charge response when there is significant amplitude for a transition at a particular  $\mathbf{q} = (q, q_{\perp})$  and  $\omega$  for a particle-hole excitation built up from the one-particle spectral weight. For example, to understand the heavily weighted amplitude at  $\mathbf{q} = (0, \pi)$ , one has to integrate over all transitions from the photoemission band in Fig. 1(a) to the inverse photoemission band in Fig. 1(b) which transfer this momentum. Since the single-particle bands are sharp and parallel, one should obtain a single well-defined peak for  $\mathbf{q} = (0, \pi)$ , which we see in Fig. 10(a) by considering excitations between the  $\omega < 0$ ,  $k_{\perp} = 0$  band, and the  $\omega > 0$ ,  $k_{\perp} = \pi$  band. In addition, the transition at  $\mathbf{q} = (0, \pi)$  has odd parity between the chains, and is thus allowed by the selection rules for the density operator as  $q \rightarrow 0$ . As the parallel component  $q$  is increased, one can see that

there will be a continuum of excitation energies which gets wider as  $q$  increases. The minimum excitation energy (position of the lower band) from this construction is shown in Fig. 10(a) by the line with solid dots. However, the excitation energy obtained is consistently smaller than the energy of the lowest heavily weighted band from QMC. Using the single particle bands to construct the two-particle excitations is equivalent to calculating the charge response using the lowest order ‘‘bubble’’ diagram, but with exact single-particle propagators, neglecting all particle-hole interactions. The particle-hole interactions on the rung, which are included in the rung eigenenergies, thus raise the charge excitation energy by a substantial amount<sup>22</sup>.

For  $t_{\perp}/t = 1.0$ , the charge response looks quite different. As shown in Fig. 10(b) and (c), there is substantial spectral weight for both  $q_{\perp} = 0$  and  $q_{\perp} = \pi$ . For  $\mathbf{q} \rightarrow (0, 0)$ , the density operator has even parity, causing the matrix element and thus the spectral weight to vanish, whereas at  $\mathbf{q} \rightarrow (0, \pi)$ , the density operator has odd parity so that optical transitions are allowed and there is spectral weight. In both channels, the size of the charge gap is approximately  $4t$ , and there is a broad structure of width  $\sim 7t$ . For  $q_{\perp} = 0$ , most of the spectral weight occurs as a dispersive peak whose energy increases with increasing  $q$ , whereas for  $q_{\perp} = \pi$  two peaks seem to contribute to the spectral weight distribution. The peaks are not well-defined enough over a range of  $q$  to extract a dispersion, but the upper peak is heavily weighted near  $q = \pi$ , at  $\omega \approx 9t$ .

We can qualitatively understand the broad incoherent structure of the charge response by considering particle-hole excitation in the single particle  $A(\mathbf{k}, \omega)$  in Fig. 2. There are four dispersive bands and a broad background, so there should be weight in both the  $q_{\perp} = 0$  and  $q_{\perp} = \pi$  branches of the charge response, and broad structure above a minimum excitation energy, which we see in Fig. 10(c) and (d). From the single particle bands in Fig. 3, one can estimate the minimum particle-hole excitation energy to be  $\sim 4t$ . In Fig. 10(c) and (d), the spectral weight near this minimum excitation energy is suppressed due to the particle-hole vertex. We have also carried out a calculation of charge response  $\chi_{\text{RPA}}^{00}(\mathbf{q}, \mathbf{q}', \omega)$  within the antiferromagnetic RPA approximation described above, using the SDW dispersion in Eq. (10), and also find a relatively broad structure above the charge gap for both  $q_{\perp} = 0$  and  $q_{\perp} = \pi$ . We plot the minimum excitation energy of  $\chi_{\text{RPA}}^{00}(\mathbf{q}, \mathbf{q}', \omega)$  in Fig. 10(b) and (c) as lines with solid dots. This line is located in the middle of the broad band in both plots.

The spin and charge response functions for  $t_{\perp}/t = 0.5$  show the same general features as in the isotropic ( $t_{\perp}/t = 1.0$ ) case and are therefore not shown here. The spin susceptibility  $\chi_s(\mathbf{q}, \omega)$  is also qualitatively identical to the RPA result  $\chi_{\text{RPA}}^{+-}(\mathbf{q}, \mathbf{q}, \omega)$  with a smaller spin velocity than in the  $t_{\perp}/t = 1.0$  case. The charge susceptibility  $\chi_c(\mathbf{q}, \omega)$  shows a clear dispersive band centered around the low-lying RPA excitations in the  $q_{\perp} = 0$  channel,

whose energy increases with increasing  $q$ . In the  $q_{\perp} = \pi$  channel, there is a broad structure of width  $\sim 8t$  with again two peaks in the spectral weight distribution.

#### IV. CONCLUSION

In summary, the single and two-particle dynamical properties of the two chain Hubbard model at half-filling can be understood by starting from two limits: the limit of non-interacting rungs treated exactly, which gives a good starting point for the large  $t_{\perp}$  case for which the spin-spin correlation length along the chains is less than a lattice spacing, and the limit of an antiferromagnetically ordered state, which gives a good starting point for the small  $t_{\perp}$  case when the spin-spin correlation length is large. The dynamical properties in the two regimes look quite different. For the large  $t_{\perp}$  regime, the remnants of the level transitions of the two site system representing a single rung, suitably broadened into bands, can explain the major features of the single-particle, spin and charge responses. In the small  $t_{\perp}$  case, calculations based on an antiferromagnetically ordered starting point, such as antiferromagnetic Hartree-Fock theory and spin-wave theory give a good qualitative picture of the coherent spin-wave part of the single particle spectral weight and of the two-particle spin dynamic correlation function. In addition, there is a broad incoherent band in the single particle spectral weight similar to that found in recent numerical work on the 1D and 2D systems.

We also have shown the single particle spectral weight and the spin and charge response functions for the physical relevant, isotropic case ( $t_{\perp}/t = 1.0$ ). The results are qualitatively similar to these in the small  $t_{\perp}$  region and can therefore be understood from an antiferromagnetic Hartree-Fock or spin-wave theory picture. The real ladder compounds have approximately the same coupling strength parallel to and perpendicular to the chains, and it will therefore be interesting to compare these isotropic  $t_{\perp}/t = 1.0$  results with future experiments.

#### ACKNOWLEDGMENTS

We would like to thank R. Preuss, A. Muramatsu, and W. Ziegler for helpful discussions. H.E., W.H., and R.M.N. are grateful to the Bavarian "FORSUPRA" program on high  $T_c$  research and the DFG under Grant No. Ha 1537/12-1 for financial support. D.P. acknowledges support from the EEC Human Capital and Mobility program under grant CHRX-CT93-0332, and D.J.S. from the NSF under Grant No. DMR 92-2507. The calculations were performed on Cray YMP's at the HLRZ in Jülich and at the LRZ München.

- <sup>1</sup> Z. Hiroi, M. Azuma, M. Takano, and Y. Bando, *J. Solid State Chem.*, **95**, 230 (1991).
- <sup>2</sup> D.C. Johnston *et al.*, *Phys. Rev. B* **35**, 219 (1987).
- <sup>3</sup> T.M. Rice, S. Gopalan, and M. Sigrist, *Europhys. Lett.* **23**, 445 (1993).
- <sup>4</sup> Z. Hiroi, and M. Takano, *Nature* **377**, 41 (1995).
- <sup>5</sup> E. Dagotto, J. Riera, and D.J. Scalapino, *Phys. Rev. B* **45**, 5744 (1992).
- <sup>6</sup> T. Barnes *et al.*, *Phys. Rev. B* **47**, 3196 (1993); T. Barnes and J. Riera, *Phys. Rev. B* **50**, 6817 (1994); R.S. Eccleston, T. Barnes, J. Brody, and J.W. Johnson, *Phys. Rev. Lett.* **73**, 2626 (1994).
- <sup>7</sup> S.R. White, R.M. Noack, and D.J. Scalapino, *Phys. Rev. Lett.* **73**, 886 (1994).
- <sup>8</sup> R.M. Noack, S.R. White, and D.J. Scalapino, *Phys. Rev. Lett.* **73**, 882 (1994); *Europhys. Lett.* **30** (3), 163 (1995).
- <sup>9</sup> H. Tsunetsugu, M. Troyer, and T.M. Rice, *Phys. Rev. B* **49**, 16078 (1994).
- <sup>10</sup> R.N. Silver, D.S. Sivia, and J.E. Gubernatis, *Phys. Rev. B* **41**, 2380 (1990), and references therein.
- <sup>11</sup> L. Balents, and M.P.A. Fisher, to be published, *cond-mat/9504082*.
- <sup>12</sup> R. Preuss, A. Muramatsu, W. von der Linden, P. Dietrich, F.F. Assaad, and W. Hanke, *Phys. Rev. Lett.* **73**, 732 (1994).
- <sup>13</sup> R. Preuss, A. Muramatsu, W. von der Linden, and W. Hanke, unpublished.
- <sup>14</sup> R. Preuss, W. Hanke, and W. von der Linden, to be published, *cond-mat/9412089*.
- <sup>15</sup> A. Moreo, S. Haas, A. Sandvik, and E. Dagotto, to be published, *cond-mat/9412107*.
- <sup>16</sup> W. von der Linden, R. Preuss and W. Hanke, to be published, *cond-mat/9503098*.
- <sup>17</sup> S.R. White, *Phys. Rev. B* **44**, 4670 (1991).
- <sup>18</sup> J.R. Schrieffer, X.G. Wen, and S.C. Zhang, *Phys. Rev. B* **39**, 11663 (1989).
- <sup>19</sup> A.P. Kampf and J.R. Schrieffer, *Phys. Rev. B* **42**, 7967 (1990).
- <sup>20</sup> L. Lilly, A. Muramatsu, and W. Hanke, *Phys. Rev. Lett.* **65**, 1379 (1990), and references therein.
- <sup>21</sup> I. Bose and S. Gayan, *Phys. Rev. B* **48**, 10653 (1993).
- <sup>22</sup> W. Hanke, and L.J. Sham, *Phys. Rev. Lett.* **43**, 387 (1979); *Phys. Rev. B* **21**, 4656 (1980).